Barrier lake formation due to landslide impacting a river

- A numerical study using a double layer-averaged two-phase flow model

Ji Li [a, b], Zhixian Cao [a*], Yifei Cui [c], Alistair G. L. Borthwick [d]

[a] *State Key Laboratory of Water Resources and Hydropower Engineering Science, Wuhan University, Wuhan 430072, China*

[b] *Zienkiewicz Centre for Computational Engineering, College of Engineering, Swansea University, Swansea SA1 8EN, UK*

[c] *State Key Laboratory of Hydroscience and Engineering, Tsinghua University, Beijing 100084, China*

[d] *Institute for Infrastructure and Environment, The University of Edinburgh, Edinburgh EH9 3JL, UK*

** Corresponding author: Zhixian Cao, e-mail addresses:* zxcao@whu.edu.cn

Highlights:

- A new double layer-averaged two-phase flow model is proposed for barrier lake formation due to landslide impacting a river
- Grains play a key role in driving water movement during subaqueous landslide motion and a two-phase theory is warranted
- Grain size effects are revealed, i.e., coarse grains and grain-size uniformity favour barrier lake formation
- A new threshold for barrier lake formation is proposed, based on landslide-to-river momentum ratio and grain size

Abstract

A granular landslide impacting a river may lead to the formation of a landslide dam blocking the streamflow and subsequently a barrier lake. Should a barrier lake outburst, the flood may be destructive and spell disastrous consequences downstream. The last decade or so has witnessed a number of experimental and numerical investigations on barrier lake outburst flooding, whilst studies on barrier lake formation remain rare, especially a physically enhanced and practically viable mathematical model is still missing. Generally, barrier lake formation is characterized by multi-physics, interactive processes between water flow, multi-sized sediment transport and morphological evolution. Here, a new double layer-averaged two-phase flow model is proposed, featuring a step forward compared with existing continuum models that involve a single-phase flow assumption and presume a single sediment size and also discrete models that preclude fine grains and assume narrow grain size distributions. The proposed model is first validated by laboratory experiments of waves due to landslides impacting reservoirs and landslide dam formation over dry valleys. Then it is applied to explore the complicated mechanism and threshold for barrier lake formation. The water and grain velocities are shown to be disparate, characterizing the primary role of grains in driving water movement during subaqueous landslide motion and also the need for a two-phase flow approach. The grain size effects are revealed, i.e., coarse grains and grain-size uniformity favour barrier lake formation. A new threshold condition is proposed for barrier lake formation, integrating the landslide-to-river momentum ratio and grain size effects. The present work facilitates a promising modelling framework for solving barrier lake formation, thereby underpinning the assessment of flood hazards due to barrier lakes.

Keywords: barrier lake formation; granular landslide; waves; double layer-averaged model; two-phase flow model; grain size effect; threshold condition

1. Introduction

Barrier lake formation due to landslides impacting rivers represents a typical class of fluvial processes with rapid changes in time and space. When subaerial landslides impact narrow river valleys, they may propagate as underflows. Accordingly, a vertical double-layer flow structure is formed as characterized by a subaqueous water-sediment mixture flow layer immediately above the riverbed and an upper clear-water flow layer. In general, large water waves and active sediment transport can be generated by landslides impacting river valleys. Due to rapid deposition of a large amount of sediments, a landslide dam can be formed [1-2] as the riverbed aggrades rapidly and then emerges from the water. Moreover, water waves may trigger more landslides or collapses on the opposite riverbank, which entrain more sediments into river and facilitate landslide dam formation, as evidenced by the recent Baige barrier lake in China [3]. Resulting from sustained upstream inflow and significant water-level rise, the water impounded by landslide dam may create a barrier lake, which may inundate the lands and infrastructures upstream. Furthermore, due to the rather loose structure, landslide dam formed by granular landslide is easy to burst, leading to destructive downstream floods and debris flows, often with high casualties and severe infrastructural damages [4-6]. The most common failure scenario of barrier lakes concerns overtopping flow with subsequent dam breaching and erosion [1]. Typical historical examples include the Tortum landslide dam in Turkey [7] as well as the Tangjiasha barrier lake [8] and the recent Baige barrier lake [3] in China. In fact, the post-behaviour of a barrier lake is highly correlated with its formation process. Therefore, enhanced understanding of barrier lake formation due to granular landslide impacting a river is important to public safety and risk

management [9].

Over the past few decades, numerous efforts have been devoted to study barrier lake failure and the resulting flood, including laboratory experiments [10-12] and numerical modeling studies [13-18]. However, studies on barrier lake formation remain rare. Physically, barrier lake formation involves complicated interactive processes between water flow, multi-sized sediment transport, and morphological evolution. Field observation is certainly the most straightforward approach to understanding this natural phenomenon. However, such observations are difficult to conduct due to the rapid, short-lasting, unpredictable occurrence and destructive power of landslides. Laboratory experiments in well-controlled conditions have been conducted in flumes to investigate landslides impacting water bodies [19-21]. However, these experiments have mainly focused on landslide-generated-waves, while sediment transport and morphological evolution are sparsely observed [22]. Consequently, they are not able to fully reveal the complicated mechanism underlying barrier lake formation. Comparatively, computational modelling is attractive, which has already become one of the most proactive approaches to enhancing the understanding of hydro-sediment-morphodynamic processes in fluvial rivers, reservoirs, estuaries, and oceans [23]. To date, however, there is a lack of a physically enhanced and practically viable mathematical model for barrier lake formation due to granular landslide impacting a river. In particular, sediment transport has not yet been sufficiently well resolved by existing models based on either discrete mechanics or continuum assumption. Consequently, the modelling framework for whole process flood risk management due to barrier lakes is still out of reach.

1.1. Discrete models

During the past decade, discrete models have been widely used for resolving the mechanical behaviour of landslides, such as Discrete Element Method (DEM) [24], Discontinuous Deformation Analysis (DDA) [25], Smoothed Particle Hydrodynamics (SPH) [26] and Materials Point Method (MPM) two-phase models [27]. Regarding landslides impacting water bodies, SPH models have been already applied for modelling landslide motions and the generated waves [28]. Note that MPM two-phase models [27], which are currently only used for landslide motions, can potentially be extended for barrier lake formation by applying the governing equations of water phase for river flow modelling. Moreover, discrete models for landslide motions can be coupled with the other models for water flows. Typical examples include coupled DEM models and fluid flow such computational fluid dynamics (CFD) models [29], SPH models [30] and Lattice-Boltzmann Method (LBM) [31] as well as coupled DDA-SPH models [32-33]. However, constrained by the excessive computational cost, a convention in discrete models is to introduce unjustified assumptions in terms of sediment transport. First, most discrete models essentially exclude fine grains. Specifically, DEM models [29-30] usually employ coarse grain models [35-36], in which upscaled grains with a size larger than real cases are used. Besides, DDA models [32-33] presume that landslides are composed of several large blocks. Such practices are physically unjustified as coarse grains can settle faster than finer grains under a given flow condition. Second, discrete models adopt much narrower grain size distributions (e.g., DEM-CFD models [29]) or even presume a single sediment size (e.g., MPM two-phase models [27], SPH models [28] and DDA-SPH models [32-33]) due to restricted shape functions used for fluid-solid interaction. However, the sediments in landslides may be highly

heterogeneous with widely distributed sizes, ranging from clay size (10^{-5} m) to boulder size (10^{1} m) [36]. Moreover, excess pore pressure is found to be influenced by grain size distribution (GSD) [37], which plays a critical role in landslide behaviors. Therefore, grain size data reveals the oversimplification of the models that presume narrow grain size distributions or a single sediment size, and they also reinforce the notion that grain-size heterogeneity may be critical to barrier lake formation due to granular landslides impacting rivers [38]. Third, mass exchange with the bed has not been fully accounted for by discrete models. Specifically, sediment erosion has not been modelled by these models except for a few cases by a single DEM model [39], while the static sediment layer is regarded as sediment deposit during the simulation [29].

1.2 Continuum models

As far as continuum models are concerned, double layer-averaged models hold great promise for resolving barrier lake formation due to their ability to reflect the two-way coupling between landslide motions and water flows [40] and the sensible balance between their theoretical integrity and applicability [22]. Double layer-averaged models employ two sets of governing equations to describe the lower water-sediment mixture flow (landslide) layer and the upper clear-water flow layer. However, existing double layer-averaged models have suffered from some major short-comings.

First, existing double layer-averaged models [22, 41-43] are based on a single-phase flow premise, in which the water-sediment mixture in the lower flow layer are regarded as a single-phase flow. Therefore, the velocities of the sediment phases in the lower flow layer are

assumed to be equal to the mixture velocity. Consequently, the relative motions and interactions between water and sediment phases are not incorporated explicitly. Indeed, this practice is only applicable for sediment-laden flow with sufficiently low sediment concentrations, in which the water phase dominates and the interphase and inter-grain size interactions are rather weak [23]. By contrast, landslides are primarily characterized by rather high sediment concentrations, characterizing the dominant role of sediment phases and the existence of strong interactions between water and sediment phases. Even intuitively, sediment phases may drive the water movement during landslide motions. In this regard, a two-phase flow theory is certainly the way forward [44] and a double layer-averaged two-phase flow model is therefore warranted.

Second, existing double layer-averaged models [22, 41-43] are confined to single-sized sediment transport (i.e., the sediment size is kept at a single value, normally the median or mean sediment diameter, throughout the simulation). Clearly, the models that assume a single sediment size do not reflect the nature of landslides, which are typically characterized by broad grain size distributions.

Third, most double layer-averaged models [41, 43] ignore mass exchange with the bed. Consequently, they cannot model the deposition process of landslide materials, which is vital to barrier lake formation. Note that the double layer-averaged model by Liu and He [42] incorporated the mass exchange with the bed. However, an additional term, which denotes a real (rather than apparent) momentum exchange with the bed, was incorrectly added into the momentum conservation equations. Physically, no real momentum exchange can be involved into mass exchange with the bed, as highlighted by Cao et al. [23]. The consequence of this

159 extra term can be serious. For example, according to Liu and He [42], the riverbed is eroded
160 by subaqueous landslide instead of being deposited, which is questionable from physical
161 intuition. Arguably, this is why this model has not yet been validated by any observed data.

162 Furthermore, most double layer-averaged models [41-43] are based on the assumption of
163 a constant sediment concentration in the lower water-sediment mixture flow layer. However,
164 sediment concentration generally varies in time and space. Strictly, this assumption is far
165 from justified. In general, sediment concentration is an unknown variable that must be
166 resolved numerically, whereas in these double layer-averaged models [41-43], its value is
167 specified a priori, which inevitably introduces uncertainties. From a physical perspective, this
168 assumption leads to a violation of the fundamental mass conservation law for sediments.
169 Moreover, this assumption can lead to serious unphysical oscillations of numerical results
170 [45]. In addition, landslides impacting rivers usually take place over irregular and possibly
171 steeply sloping beds. The common assumption of low slopes in shallow water hydrodynamic
172 models is no longer valid, and the effects of steep slopes on sediment transport must not be
173 neglected. However, only a few double layer-averaged models [43] have ever considered the
174 effects of steep slopes on landslide motions but unjustifiably neglect their effects when
175 modelling water flows.

176 *1.3 Present work*

177 In this study, a double layer-averaged two-phase flow model is proposed for barrier lake
178 formation due to landslide impacting a river. Specifically, one set of layer-averaged
179 single-phase flow equations is introduced to describe the upper clear-water flow layer, while

another set of layer-averaged two-phase flow equations is deployed to describe the subaqueous water-sediment mixture flow layer. The governing equations of the model are established in a global Cartesian coordinate system with two axes within the horizontal plane and one axis in the vertical direction. To account for the effects of steep slopes, the concept of projected gravity proposed by Juez et al. [46] is incorporated. Compared to existing models based on discrete mechanics or continuum assumption, the model features a step forward by explicitly incorporating multi grain sizes, sediment mass conservation, mass exchange with the bed and interphase and inter-grain size interactions. A new numerical algorithm is proposed. Specifically, within the new model, the governing equations for each moving layer are cast into a non-homogeneous hyperbolic system. The two hyperbolic systems of the governing equations for the two layers are solved separately and synchronously. Each hyperbolic system is solved by a quasi-well-balanced finite volume Slope Limiter Centred (SLIC) scheme. The model is validated by laboratory experiments on waves due to granular landslides impacting reservoirs [21] and landslide dam formation over dry valleys [47]. Then it is applied to explore the underlying complicated mechanism and the threshold for barrier lake formation due to granular landslide impacting a river.

2. Mathematical model

2.1. Governing equations

Consider shallow water-sediment flows over an erodible bed composed of non-cohesive sediment with N size classes. Let d_k denote the diameter of the k th sediment size, where

subscript $k=1,2,.....,N$. The proposed model is developed by coupling the recent double layer-averaged single-phase flow model [22] and the depth-averaged two-phase flow model [48-50]. Here, “depth-averaged” or “layer-averaged” refers to the fact that the physical quantities (velocity and volume fraction) are integrated and averaged along the depth of the flow. Moreover, the shape factor, which arises from the depth-averaging procedure and represents the effects of non-uniformity of vertical structure of velocity and sediment concentration, are presumed to be unit. Indeed, it is a conventional practice in shallow water-sediment models [53], which implies the effects of shape factors are neglected. However, this practice does not mean that velocity and sediment concentration are assumed to be constant along the flow depth. The model is established in a global Cartesian coordinate system and uses the projected gravity concept [46] to account for the effect of steep slopes. In general, interactions occur between the upper clear-water flow layer, the water and sediment phases in the lower flow layer and the erodible bed, which are characterized by mass and momentum exchanges. The coupled modelling approach is generally justified and thus implemented [51]. The governing equations essentially comprise the mass and momentum conservation equations for the clear-water flow layer, the water-sediment mixture, the water and sediment phases in the lower water-sediment mixture flow layer, and the mass conservation equations for the bed sediment.

For the upper clear-water flow layer:

$$\frac{\partial \rho_w h_w}{\partial t}+\frac{\partial \rho_w h_w u_w}{\partial x}+\frac{\partial \rho_w h_w v_w}{\partial y}=-\rho_w E_w \tag{1}$$

221 $$\frac{\partial \rho_w h_w u_w}{\partial t}+\frac{\partial}{\partial x}(\rho_w h_w u_w^2+0.5\rho_w g_{\psi_w} h_w^2)+\frac{\partial \rho_w h_w u_w v_w}{\partial y}=-\rho_w g_{\psi_w} h_w \frac{\partial \eta_s}{\partial x}-\rho_w E_w u_w-\tau_{wx} \quad (2)$$

222 $$\frac{\partial \rho_w h_w v_w}{\partial t}+\frac{\partial \rho_w h_w v_w u_w}{\partial x}+\frac{\partial}{\partial y}(\rho_w h_w v_w^2+0.5\rho_w g_{\psi_w} h_w^2)=-\rho_w g_{\psi_w} h_w \frac{\partial \eta_s}{\partial y}-\rho_w E_w v_w-\tau_{wy} \quad (3)$$

223 For the lower water-sediment mixture flow layer:

224 $$\frac{\partial \rho_m h_m}{\partial t}+\frac{\partial \rho_m h_m u_m}{\partial x}+\frac{\partial \rho_m h_m v_m}{\partial y}=\rho_w E_w-\rho_0 \frac{\partial z_b}{\partial t} \quad (4)$$

225 $$\begin{aligned}\frac{\partial \rho_m h_m u_m}{\partial t}+\frac{\partial}{\partial x}(\rho_m h_m u_m^2+0.5\rho_m g_{\psi_m} h_m^2)+\frac{\partial \rho_m h_m u_m v_m}{\partial y}&=-\rho_m g_{\psi_m} h_m \frac{\partial z_b}{\partial x}-\rho_w g_{\psi_w} h_m \frac{\partial h_w}{\partial x}+\rho_w E_w u_w\\ &+\tau_{wx}-\tau_{bx}-\frac{\partial}{\partial x} h_m \sum[\rho_s c_k i_{s_k x}(i_{s_k x}-i_{fx})]\\ &-\frac{\partial}{\partial y} h_m \sum[\rho_s c_k i_{s_k x}(i_{s_k y}-i_{fy})]\end{aligned} \quad (5)$$

226 $$\begin{aligned}\frac{\partial \rho_m h_m v_m}{\partial t}+\frac{\partial \rho_m h_m u_m v_m}{\partial x}+\frac{\partial}{\partial y}(\rho_m h_m v_m^2+0.5\rho_m g_{\psi_m} h_m^2)&=-\rho_m g_{\psi_m} h_m \frac{\partial z_b}{\partial y}-\rho_w g_{\psi_w} h_m \frac{\partial h_w}{\partial y}+\rho_w E_w v_w\\ &+\tau_{wy}-\tau_{by}-\frac{\partial}{\partial y} h_m \sum[\rho_s c_k i_{s_k y}(i_{s_k y}-i_{fy})]\\ &-\frac{\partial}{\partial x} h_m \sum[\rho_s c_k i_{s_k y}(i_{s_k x}-i_{fx})]\end{aligned} \quad (6)$$

227 For the size-specific sediment phase in the lower water-sediment mixture layer:

228 $$\frac{\partial \rho_s h_{sk}}{\partial t}+\frac{\partial \rho_s h_{sk} u_{sk}}{\partial x}+\frac{\partial \rho_s h_{sk} v_{sk}}{\partial y}=\rho_s F_k \quad (7)$$

229 $$\begin{aligned}\frac{\partial \rho_s h_{sk} u_{sk}}{\partial t}+\frac{\partial}{\partial x}(\rho_s h_{sk} u_{sk}^2+\frac{1}{2}c_k \rho_m g_{\psi_m} h_m^2)+\frac{\partial}{\partial y}(\rho_s h_{sk} u_{sk} v_{sk})&=-\rho_m g_{\psi_m} h_{sk} \frac{\partial z_b}{\partial x}-\rho_w g_{\psi_w} h_{sk} \frac{\partial h_w}{\partial x}\\ &-\tau_{s_k bx}+\tau_{wx} c_k+F_{s_k fx}+F_{s-s_k x}\\ &+\frac{1}{2}\rho_m g_{\psi_m} h_m^2 \frac{\partial c_k}{\partial x}\end{aligned} \quad (8)$$

230 $$\begin{aligned}\frac{\partial \rho_s h_{sk} v_{sk}}{\partial t}+\frac{\partial}{\partial x}(\rho_s h_{sk} u_{sk} v_{sk})+\frac{\partial}{\partial y}(\rho_s h_{sk} v_{sk}^2+\frac{1}{2}c_k \rho_m g_{\psi_m} h_m^2)&=-\rho_m g_{\psi_m} h_{sk} \frac{\partial z_b}{\partial y}-\rho_w g_{\psi_w} h_{sk} \frac{\partial h_w}{\partial y}\\ &-\tau_{s_k by}+\tau_{wy} c_k+F_{s_k fy}+F_{s-s_k y}\\ &+\frac{1}{2}\rho_m g_{\psi_m} h_m^2 \frac{\partial c_k}{\partial y}\end{aligned} \quad (9)$$

For the water phase in the lower water-sediment mixture layer:

$$\frac{\partial \rho_w h_f}{\partial t}+\frac{\partial \rho_w h_f u_f}{\partial x}+\frac{\partial \rho_w h_f v_f}{\partial y}=\rho_w p\frac{F_T}{1-p} \tag{10}$$

$$\begin{aligned}\frac{\partial \rho_w h_f u_f}{\partial t}+\frac{\partial}{\partial x}(\rho_w h_f u_f^2+\frac{1}{2}c_f\rho_m g_{\psi_m} h_m^2)+\frac{\partial}{\partial y}(\rho_w h_f u_f v_f)=&-\rho_m g_{\psi_m} h_f\frac{\partial z_b}{\partial x}-\rho_w g_{\psi_w} h_f\frac{\partial h_w}{\partial x}\\ &-\tau_{fbx}+\tau_{wx}c_f-\sum F_{s_k fx}\\ &+\frac{1}{2}\rho_m g_{\psi_m} h_m^2\frac{\partial c_f}{\partial x}\end{aligned} \tag{11}$$

$$\begin{aligned}\frac{\partial \rho_w h_f v_f}{\partial t}+\frac{\partial}{\partial x}(\rho_w h_f u_f v_f)+\frac{\partial}{\partial y}(\rho_w h_f v_f^2+\frac{1}{2}c_f\rho_m g_{\psi_m} h_m^2)=&-\rho_m g_{\psi_m} h_f\frac{\partial z_b}{\partial y}-\rho_w g_{\psi_w} h_f\frac{\partial h_w}{\partial y}\\ &-\tau_{fby}+\tau_{wy}c_f-\sum F_{s_k fy}\\ &+\frac{1}{2}\rho_m g_{\psi_m} h_m^2\frac{\partial c_f}{\partial y}\end{aligned} \tag{12}$$

For the bed deformation:

$$\frac{\partial z_b}{\partial t}=-\frac{F_T}{1-p} \tag{13}$$

where t is time; x and y are the horizontal coordinates; η_s is the elevation of the interface between the upper clear-water flow layer and the lower water-sediment mixture flow layer; h_w is the thickness of the clear-water flow layer; u_w and v_w are the layer-averaged velocity components of the clear-water flow layer in the $x-$ and $y-$ directions; f, s and m denote the water phase, the sediment phase, and the water-sediment mixture in the lower layer; h_m is the thickness of the lower water-sediment mixture flow layer; $h_{sk}=h_m c_k$ is the size-specific thickness of the sediment phase in the lower flow layer; z_b is the bed elevation; c_k is the layer-averaged size-specific volumetric sediment concentration of the lower flow layer; $c_T=\sum c_k$ is the layer-averaged total sediment concentration; $c_f=1-c_T$ is the layer-averaged volume fraction of the water phase

of the lower flow layer; ρ_w and ρ_s are the pure densities of the water and sediment phases respectively, $\rho_m = \rho_s c_T + \rho_f (1 - c_T)$ is the density of the water-sediment mixture in the lower flow layer; $\rho_0 = \rho_s (1-p) + \rho_f p$ is the density of the bed; p is the bed sediment porosity, and thus $1-p$ is the volumetric sediment concentration of the stationary bed; u_{sk} and v_{sk} are the size-specific layer-averaged velocity components of the sediment phase in the lower flow layer; u_f and v_f are the layer-averaged velocity components of the water phase in the lower flow layer; u_m and v_m are the layer-averaged velocity components of the water-sediment mixture in the lower flow layer; u_m and v_m are defined as $\rho_m u_m = \sum (\rho_s u_{s_k} c_k) + \rho_f u_f (1 - c_T)$ and $\rho_m v_m = \sum (\rho_s v_{sk} c_k) + \rho_f v_f (1 - c_T)$, according to mass flux conservation; $i_{s_k x} = u_{sk} - u_m$ and $i_{fx} = u_f - u_m$ denote the differences among the size-specific sediment velocity u_{sk}, the water velocity u_f and the water-sediment mixture velocity u_m in the $x-$ direction, while $i_{s_k y} = v_{sk} - v_m$ and $i_{fy} = v_f - v_m$ denote their counterparts in the $y-$ direction; τ_{wx} and τ_{wy} are the bottom shear stress components for the clear-water flow layer; τ_{bx} and τ_{by} are the bottom shear stress components for the lower water-sediment mixture flow layer; $\tau_{s_k bx}$ and $\tau_{s_k by}$ are the size-specific solid resistance components in the lower flow layer; τ_{fbx} and τ_{fby} are the size-specific fluid resistance components in the lower flow layer; $F_{s_k fx}$ and $F_{s_k fy}$ are the size-specific layer-averaged interphase interaction force components; $F_{s-s_k x}$ and $F_{s-s_k y}$ are the size-specific layer-averaged inter-grain size interaction force components, which are exerted on sediment phase k by the other constituents of sediment phases and $\sum (F_{s-s_k x}) = 0$, $\sum (F_{s-s_k y}) = 0$; E_w is the mass flux of the water entrainment across the interface between two moving layers; F_k is the size-specific net flux of sediment exchange with the bed and

$F_T = \sum F_k$. $g_{\psi_w} = g\cos^2\psi_w$ and $g_{\psi_m} = g\cos^2\psi_m$ are the corrected gravitational accelerations for the clear-water flow layer and the lower water-sediment mixture flow layer, where g is the gravitational acceleration and ψ_w and ψ_m are the angles of the interface and the bed, defined as $\cos\psi_w = 1/\sqrt{1+(\partial\eta_s/\partial x)^2+(\partial\eta_s/\partial y)^2}$ and $\cos\psi_m = 1/\sqrt{1+(\partial z_b/\partial x)^2+(\partial z_b/\partial y)^2}$, according to Juez et al. [46].

For multi grain sizes, the concept of the active layer presented by Hirano [52], which has been widely used in the context of fluvial hydraulics [53], is adopted to evaluate bed grain size stratigraphic evolution. By analogy to fluvial hydraulics [52, 54-55], this concept is based on a three-layer structure, composed of the water-sediment mixture flow layer, the active layer, and the substrate layer. The active layer is located between the water-sediment mixture flow layer and the substrate layer. Sediments within the active layer are assumed to be well mixed in the vertical direction and can exchange freely with the upper and lower layers. The substrate layer, known as the stratigraphy of the deposit, has a certain structure and may vary over time. Physically, the active layer equation is based on the size-specific mass conservation of the bed sediments. In general, three critical parameters are involved, i.e., the active layer thickness, the size-specific sediment exchange between the water-sediment mixture layer and the bed, and the sediment fraction at the lower interface of the active layer. Accordingly, the active layer equation is

$$\frac{\partial h_a f_{ak}}{\partial t} + f_{Ik}\frac{\partial \xi}{\partial t} = -\frac{F_k}{1-p} \tag{14}$$

where h_a is the thickness of the active layer; f_{ak} is the fraction of the kth size sediment in the active layer such that $\sum f_{ak} = 1$; $\xi = z_b - h_a$ is the elevation of the bottom surface of

290 the active layer; and f_{Ik} is the fraction of the k th size sediment in the interface between the
291 active layer and the substrate layer, where $\sum f_{Ik} = 1$. In this study, the active layer thickness
292 $h_a = 2d_{84}$ is used following the convention in fluvial hydraulics [56], where $d_{84} =$ is the
293 grain size at which 84% of the sediments are finer. As shown in Eq. (14), the net flux of
294 sediment exchange [i.e., the right hand side (RHS) of Eq. (14)] accounts for the variation in
295 the fraction of the active layer [i.e., the first term on the left hand side (LHS) of Eq. (14)] and
296 the change in the sediment content due to movement of the interface between the active layer
297 and its substrate [i.e., the second term on the LHS of Eq. (14)]. Moreover, the bed
298 deformation equation, i.e., Eq. (13) can be readily obtained by integrating Eq. (14) over all
299 grain sizes, due to the fact that $\sum f_{ak} = 1$ and $\sum f_{Ik} = 1$.

300 To close the governing equations of the proposed double layer-averaged two-phase flow
301 model, a set of relationships must be introduced to determine the sediment exchange fluxes,
302 the shear stresses, the water entrainment, and the interaction forces, which are described in
303 detail in Text S1 (see Supplementary materials). Estimation of sediment exchange with the
304 bed is one of the key components of computational models of geophysical mass flows (e.g.,
305 landslides, debris flows, and avalanches). However, an understanding of the physical
306 processes underlying geophysical mass flows remains unclear [57-58]. Therefore, the widely
307 used closure model in fluvial hydraulics [53] is employed to estimate the mass exchange with
308 the bed. This closure model [53, 59-60] has been shown to perform well in modelling debris
309 flows [48] and landslides [22], and so is adopted in this study. In short, two distinct
310 mechanisms are generally involved in mass exchange with the bed: upward bed sediment
311 entrainment due to interphase and inter-grain size interactions and downward sediment

312 deposition as the result of primarily gravitational action. Following the conventional practice
313 in two-phase flow modelling, the total bed shear stresses for the water-sediment mixture in
314 the lower flow layer are divided into the bed shear stress components exerted respectively on
315 the water and sediment phases [61-63]. The solid resistance is determined by the Coulomb
316 friction law [64], which expresses the collinearity of shear stress and normal stress through a
317 friction coefficient. The fluid resistance is estimated using Manning's equation. Similarly, the
318 bottom shear stress for the clear-water flow layer is also estimated by Manning's equation
319 [43]. The mass flux of water entrainment E_w, which represents the mixing of the lower
320 water-sediment mixture flow layer with the upper clear-water flow layer across the interface
321 of the two moving layers, is determined by a slightly adapted version of the relationship
322 originally proposed for turbidity currents [65]. The interphase drag force is determined by
323 combining the Ergun equation for dense water-sediment mixtures and the power law for
324 dilute suspensions [66], while the inter-grain size interaction drag force includes a linear
325 velocity-dependent drag force, a inter-grain size surface interaction force and a remixing
326 force [67-68]. All the empirical relationships presented above to close the present model are
327 not new at all in the general field of shallow water hydro-sediment-morphodynamics. Indeed,
328 to date, there are no generally valid formulations available for representing sediment
329 exchange fluxes, shear stresses, water entrainment, and interaction forces. While uncertainly
330 is inevitably introduced, it can be carefully addressed by means of sensitivity computations
331 and analyses, a common practice in almost all computational models for shallow
332 water-sediment flows.

333 *2.2. Numerical algorithm*

Eqs. (1-14) form a nonlinear system of fourteen partial differential equations, which is currently too complicated to be solved numerically as a single system. Here a new numerical algorithm is proposed. Following the numerical strategy proposed by Cao et al. [69], Eqs. (1-12) can be divided into two reduced-order systems representing the clear-water flow layer (Eqs. 1-3) and the lower water-sediment mixture flow layer (Eqs. 4-12), whereas the bed deformation equation (Eq. 13) and the active layer equation (Eq. 14) are solved separately from the remaining equations. Besides, regarding the mathematical model for the lower water-sediment mixture flow layer, only two of the three governing equation systems for the water-sediment mixture (Eqs. 4-6), the sediment phase (Eqs. 7-9) and the water phase (Eqs. 10-12) are independent and can in principle be used. As suggested by Li et al. [48-50], the governing equation system for the lower water-sediment mixture flow layer is composed of the equations for the water-sediment mixture (Eqs. 4-6) and the sediment phase (Eqs. 7-9) because this system is hyperbolic and characterized by the straightforward derivation of the real and distinct eigenvalues.

In summary, the proposed double layer-averaged two-phase flow model involves eleven variables, including the thickness h_w and layer-averaged velocity components u_w and v_w of the clear-water flow layer; the thickness h_m and layer-averaged velocity components u_m and v_m of the lower water-sediment mixture flow layer; the size-specific thickness h_{sk} and layer-averaged velocity components u_{sk} and v_{sk} of the sediment phase in the lower layer; the bed elevation z_b; and the fraction of the kth size sediment in the active layer f_{ak}. Correspondingly, the proposed model is composed of eleven governing equations, including the complete mass and momentum conservation equations for the upper clear-water flow

356 layer (Eqs. 1-3) and the water-sediment mixture in the lower flow layer (Eqs. 4-6), the
357 size-specific mass and momentum conservation equations for the sediment phase in the lower
358 flow layer (Eqs. 7-9), the bed deformation equation (Eq. 13) and the active layer equation (Eq.
359 14). Within this model, the two systems representing the clear-water flow layer (Eqs. 1-3) and
360 the lower water-sediment mixture flow layer (Eqs. 4-9) can be proven to be hyperbolic [70].
361 Therefore, they can be solved separately and synchronously by a quasi-well-balanced finite
362 volume SLIC scheme, which is adapted from the numerical algorithm in Cao et al. [71] and is
363 described in Text S2 in the Supplementary materials. In general, two types of boundaries, i.e.
364 open and closed boundaries, are involved in this work. At an open boundary, such as the inlet
365 or outlet of a channel, the method of characteristics is used for subcritical flow conditions to
366 obtain the updated values of flow variables, which however should be directly prescribed at
367 the inlet and set to be zero gradients at the outlet for supercritical flows. The depth-averaged
368 sediment concentration c_k at an open boundary, however, needs to be specified. At a closed
369 boundary, such as the side walls of a channel, a free-slip and non-permeable condition is
370 employed [72].

371 The double layer-averaged two-phase flow model equations along with the model
372 closures and the numerical algorithm have been presented above. Essentially, the proposed
373 model has incorporated the leading-order physical factors in the mass and momentum
374 conservation equations, such as gravitation, resistance, inter-phase and inter-grain size
375 interactions. It is appreciated that more delicate and refined mechanisms may exist in
376 sediment-laden flows and modify the modelling results (e.g., viscous particle resuspension
377 [73] and shear-induced particle migration [74]). Yet these are presumably second- and

higher-order factors, and it is sensible to have these reserved for incorporation in the model in the future.

2.3 Comparison with previous models

Table 1 compares the key physics and computational efficiency of the present and previous models, which can be applied to barrier lake formation due to landslide impacting a river. Physically, compared to existing models based on discrete mechanics [27-29, 32-33] or continuum assumption [22], the present model features a physical step forward. Specifically, compared to MPM two-phase models [27], SPH models [28], DEM-CFD models [29], DDA-SPH models [32-33] that exclude fine grain, presume narrower grain size distributions or a single sediment size, and incompletely consider mass exchange with the bed, the present model is extended due to the incorporation of multi grain sizes and mass exchange with the bed. In comparisons with the double layer-averaged single-phase flow model by Li et al. [22], the present model is physically enhanced without evoking the presumption of equal solid and fluid velocities embedded in a single-phase flow model for the sediment-laden layer, explicitly incorporating multi grain sizes as well as interphase and inter-grain size interactions.

Regarding computational efficiency, depth-averaged models within the framework of shallow water hydrodynamics are the most efficient. Comparatively, discrete models such as SPH models, DEM-CFD models and DDA-SPH models generally require excessively high computational costs as they involve the calculation of the interactions of multiple discrete bodies with continuously changing contacts. MPM two-phase models lie between

depth-averaged models and discrete models due to the hybrid Lagrangian and Eulerian descriptions and the involved mesh-free techniques. If MPM two-phase model is to be extended for barrier lake formation, higher dimensional shape functions are required for the lower water-sediment mixture flow layer in landside-river interactions, which significantly increase the computational time.

Table 1 Comparisons of key physics and computational efficiency of the present and previous models

Models	References	Physics			Computational efficiency
		Multi grain sizes	Mass exchange with the bed	Interphase and inter-grain size interactions	
SPH models	Shi et al. [28]	×	×	√	Low
DEM-CFD models	Zhao et al. [29]	×	×	√	Low
DDA-SPH models	Wang et al. [32-33]	×	×	√	Low
MPM two phase models	Bandara and Soga [27]	×	×	√	Medium
Double layer-averaged single-phase flow models	Li et al. [22]	×	√	×	High
Double layer-averaged two-phase flow model	Present	√	√	√	High

3. Computational case studies

The present double layer-averaged two-phase flow model is first validated by laboratory experiments on waves due to granular landslides impacting reservoirs [21] and landslide dam formation over dry valleys [47]. Then, based on numerical case studies, the model is applied to explore the complicated mechanism and the threshold for barrier lake formation due to landslides impacting rivers.

Here, a fixed uniform mesh is used for each case, with spatial steps sufficiently fine to ensure mesh independence of the solution, i.e. essentially equivalent solutions are obtained with an even finer mesh. The friction angle $\delta =$ 30º. The empirical weighting parameter φ, which usually varies between 0.61 and 0.81 based on the sediment size [75], is calibrated to be 0.65 for the present computational cases. A unified and constant value of the modification coefficient ϕ (= 1) is used for all the cases. Unless otherwise specified, the values of the other common parameters are $\rho_f =$ 1000 kg/m^3, $\rho_s = 2650$ kg/m^3, and $g =$ 9.8 m^2/s, $p =$ 0.4, $Cr =$ 0.5. In this study, the transverse direction is along the center line of the sliding slope, while the longitudinal direction is along the center line of the river valley.

3.1. Waves due to granular landslides impacting reservoirs (Series 1)

In general, when granular landslide impacts a river, large waves and active sediment transport can be generated, both of which may affect barrier lake formation as evidenced by the recent Baige barrier lake in China [3]. First, a numerical simulation is undertaken of the waves driven by a granular landslide entering a reservoir, and the results are compared against laboratory data obtained by Bregoli et al. [21] whose experimental setup comprised a

landslide generator, a wave basin, and a measurement system (Fig. 1). Similar to previous experiments [19, 20], Bregoli et al. [21] only measured the landslide-generated waves, but ignored the associated sediment transport and morphological evolution. The landslide generator consisted of a steep ramp with a slope angle varying from 0° to 27.8° and a wheeled box containing granular material that slid on 6.2 m long rails fixed to the lateral walls of the flume. And the rails had a very low degree of surface roughness and deformability. On reaching the end of the ramp, the box was halted instantaneously by a high-resistance shock absorber, and the landslide material released into a rectangular basin 4.10 m long and 2.45 m wide. The location $x =$ 0 m corresponded to the point that the landslide entered the water. Water level displacements were measured at eight locations ($x =$ 1.7, 1.9, 2.1, 2.3, 2.5, 2.7, 2.9 and 3.1 m) along the central axis of the basin. This case relates to a test where the angle of the ramp slope α was 27.8°, and the initial landslide was 1 m long, 0.34 m wide, and 0.25 m deep. The landslide had an initial velocity of approximately 5.3 m/s at release. The landslide shape was assumed to remain unchanged during the acceleration of the box. The basin's initial water depth h_{w0} was set to 0.20 m. The granular materials comprised gravel of mean diameter $d =$ 16.9 mm, grain density $\rho_s =$ 2820 kg/m^3, and bulk porosity $p =$ 0.4. The Manning coefficients for bed roughness $n_b =$ 0.03 s/m$^{1/3}$ and interface roughness $n_w =$ 0.005 m$^{-1/3}$ s were calibrated to the measured wave level displacement. The computational domain included the steep ramp and the basin. The spatial steps Δx and Δy were both 0.02 m. A free-slip and non-permeable condition was employed in the boundaries (i.e., side walls) [72]. Time $t =$ 0 s coincides with the instant that the landslide was released from the box. In this case, a double layer-averaged

453 single-phase flow model [22] is also used for comparisons. For simplicity, the double
454 layer-averaged two-phase flow model and the double layer-averaged single-phase flow model
455 are respectively labelled ‘DLT’ and ‘DLS’. Note that all the modelling parameters in DLT and
456 DLS models are the same.

457 Fig. 2 shows the variations in time of the landslide velocity u_s and the thickness h_s at
458 the impact point computed by the DLT and DLS models, with the measured data from
459 Bregoli et al. [21] superimposed. Although appreciable discrepancies are observed, the
460 landslide motion predicted by the DLT model is fairly consistent with the measured data,
461 whereas the DLS results are characterized by a lower velocity and a smaller thickness. Fig. 3
462 displays the non-dimensional water level displacement time series at the eight gauges,
463 computed by the DLT and DLS models along with measured data obtained by Bregoli et al.
464 [21]. Despite the distinguishable discrepancies, the results from the DLT model agree with
465 the observed data of landslide-generated waves more closely than the DLS model. Several
466 reasons might be responsible for the discrepancies between the experimental and numerical
467 results. First, the initial conditions are difficult to be set as the same as in the experiments,
468 especially the acceleration of box and the releasing process of landslide materials, which
469 however cannot be fully considered by the proposed model. Second, the empirical
470 relationships and parameters for model closures may also inevitably bring about some
471 discrepancies.

472 Figs. 4 and 5 show the sediment concentration distribution and bed deformation in the
473 basin (where measured data are unavailable), computed by the DLT and DLS models. The
474 landslide sustains a high sediment concentration (~ 0.6) after completely entering the water

475 and spreading over the flatbed (Figs. 4 a1-a2 and Figs. 4 b1-b2). No deposition occurs during
476 this stage, mainly because the landslide has attained a sufficiently high speed from the box
477 acceleration prior to release. The computed sediment concentrations determined by the two
478 models are nearly the same. After reaching the wall at $x =$ 3.34 m, the landslide decelerates
479 gradually, resulting in a decrease in sediment concentration (Figs. 4 a3-a4 and Figs. 4 b3-b4)
480 and bed aggradation due to deposition of the landslide material (Fig. 5). Sediment
481 concentrations determined by the DLS model decrease more rapidly than those determined by
482 the DLT model. Consequently, the DLS model is characterized by a more rapid sediment
483 deposition speed and a larger bed depositional area compared to the DLT model.

484

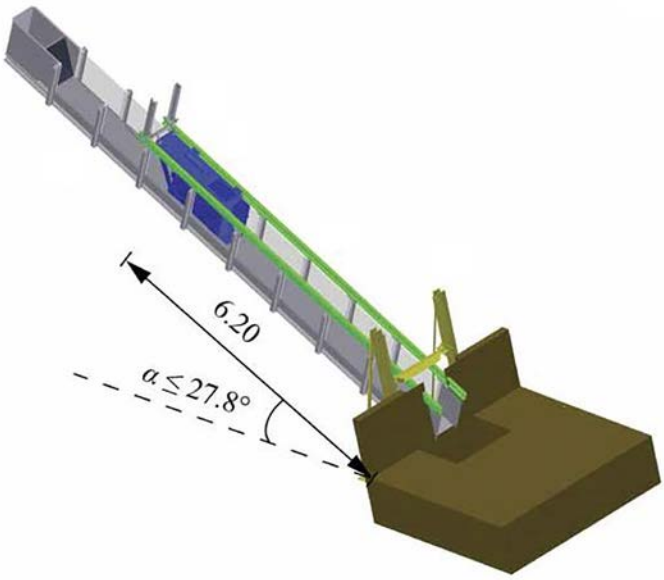

485

486 **Fig. 1.** Experimental setup for Series 1 (adapted from Bregoli et al. [21])

487

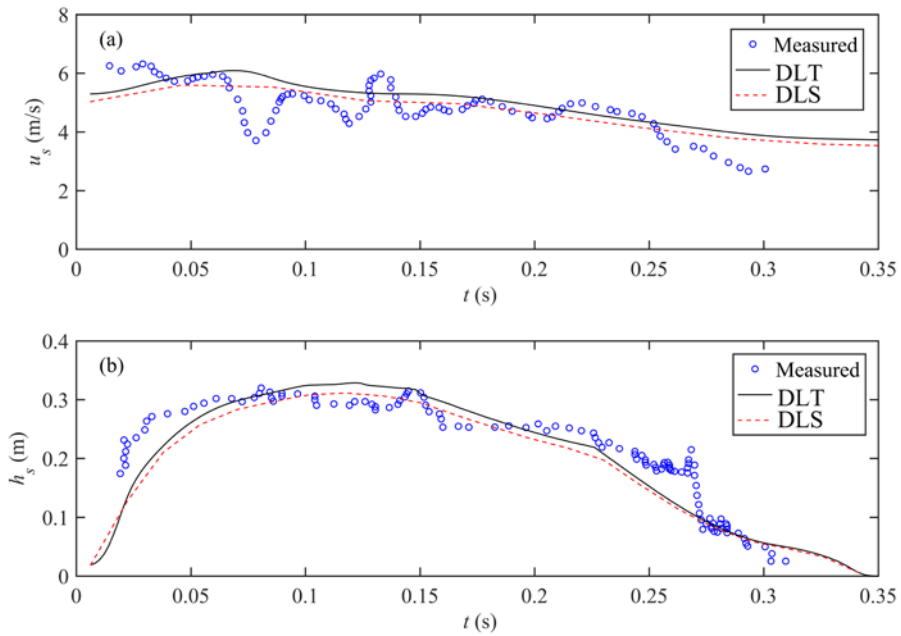

Fig. 2. Granular landslide into a reservoir: DLT and DTS predictions and Bregoli et al.'s [21] measurements of temporal variations of (a) landslide velocity and (b) landslide thickness at impact with water in a basin.

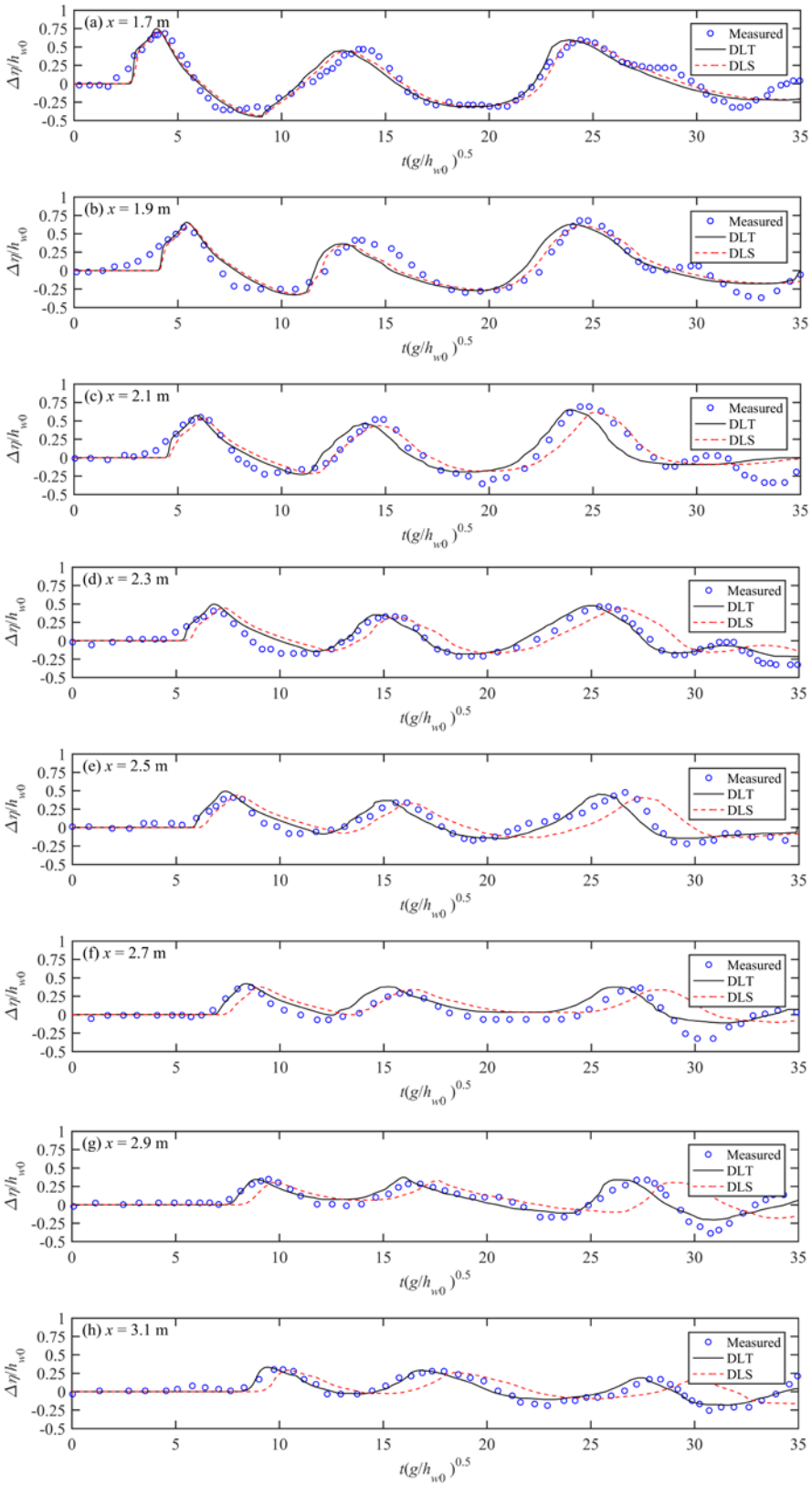

Fig. 3. Granular landslide into a reservoir: DLT and DTS model predictions and Bregoli et al.'s [21] measurements of non-dimensional water level displacements with non-dimensional time water in a basin.

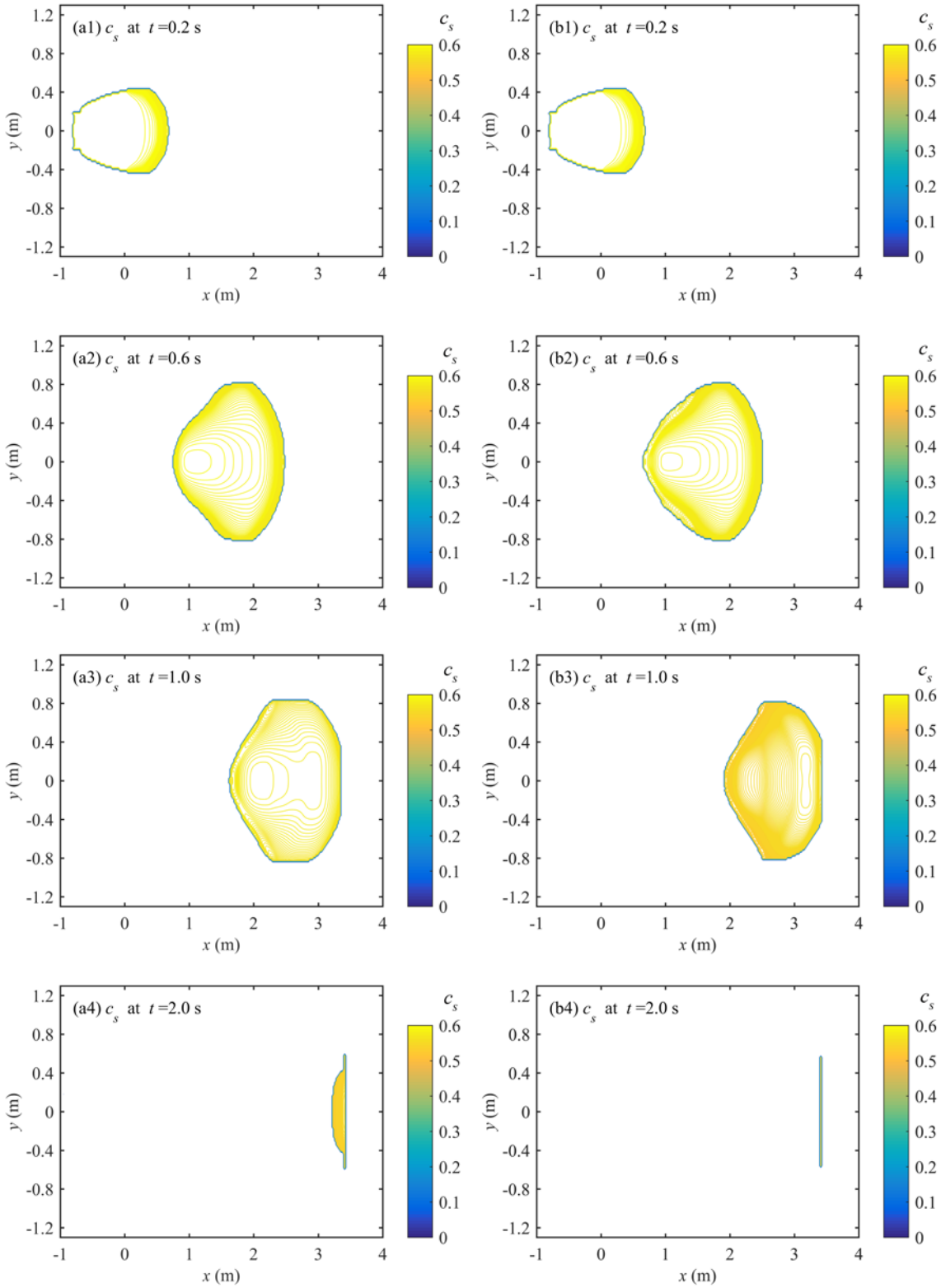

Fig. 4. Granular landslide into a reservoir: (a1-a4) DLT and (b1-b4) DLS model predictions of sediment concentration distributions in the basin.

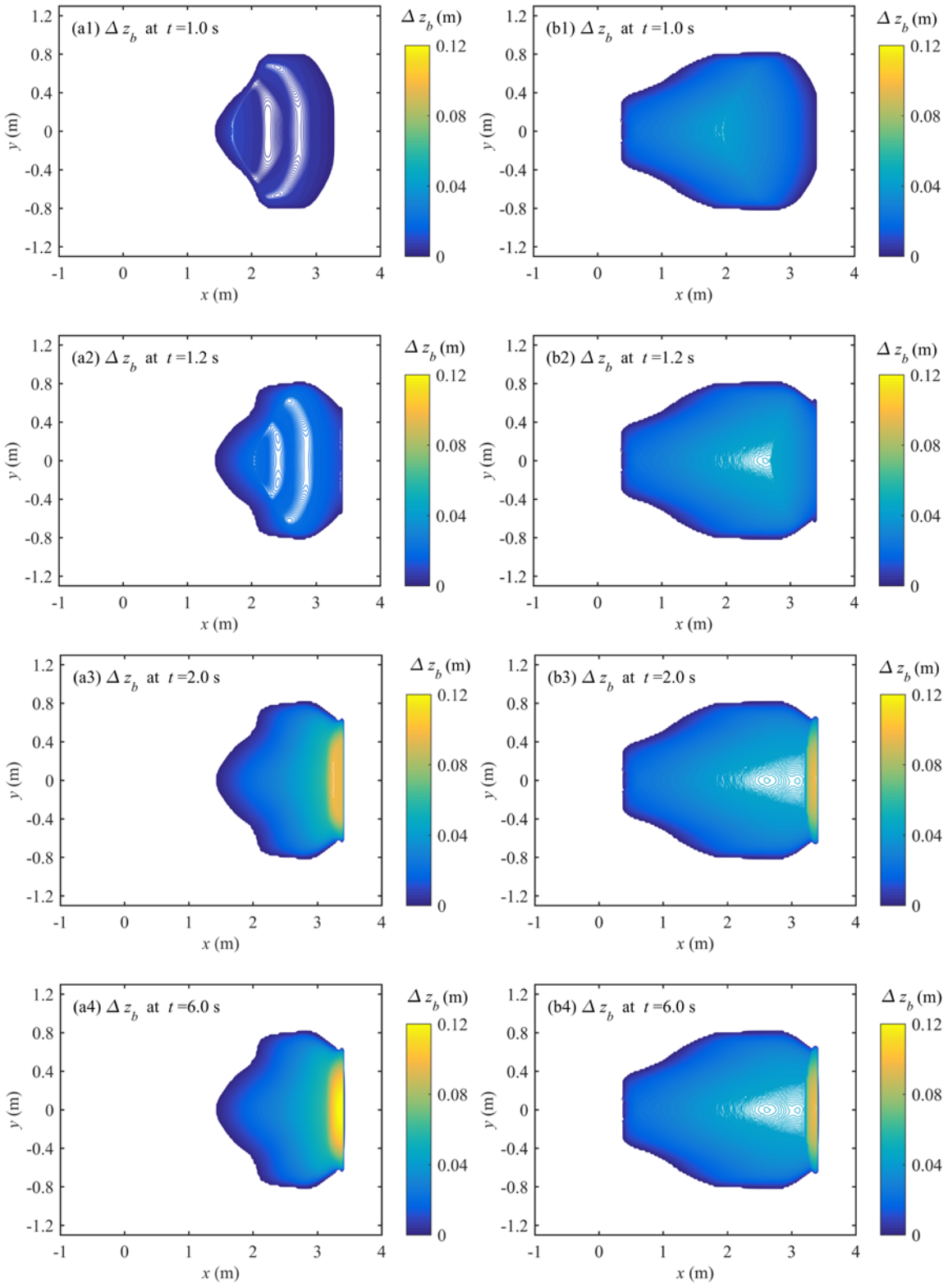

Fig. 5. Granular landslide into a reservoir: (a1-a4) DLT and (b1-b4) DLS model predictions of bed deformation in the basin.

506 *3.2. Landslide dam formation over dry valleys (Series 2)*

507 Next, landslide slide formation over dry valleys due to a sudden release of granular
508 materials are considered, based on a series of flume experiments documented by Zhao et al.
509 [47]. In these experiments, to simplify the processes of landslide initiation and acceleration,
510 the landslide body was given a certain initial velocity to shorten the acceleration process and
511 the initial shape of the landslide was assumed to be regular block and the sliding path was
512 constrained in a sliding groove rather than a free slope surface. The geometry of the sliding
513 groove was 1 m × 1 m × 0.6 m with a slope angle of 30°. A valley was installed at the end of
514 the sliding groove (Fig. 6). The length of the valley was 3 m. The effects of three main
515 variables, including initial landslide velocity, valley shape (Fig. 7) and valley bed inclination,
516 on landslide dam morphology were investigated. The surface slope of landslide dam was
517 measured, which refers to the angle between the dam surface and the horizontal plane. φ_u
518 was defined as the angle in the upstream direction, while φ_d was defined as the angle in the
519 downstream direction. Table 2 summarizes the initial conditions of all the experimental cases.
520 The computational domain included the sliding groove and the dry valley. The spatial steps
521 Δx and Δy were both 0.02 m. Numerical modelling was performed within the time period
522 before the landslide reached the boundaries, where the boundary conditions can be simply set
523 at the initial static status. Time $t =$ 0 s coincides with the instant that the landslide was
524 released from the groove. The Manning coefficients for bed roughness $n_b =$ 0.02 s/m$^{1/3}$ and
525 interface roughness $n_w =$ 0.005 m$^{-1/3}$ s were calibrated to the measured data.

526 To demonstrate the performance of the model, all the experimental cases listed in Table
527 2 were revisited. Table 2 also includes the computed upstream surface slope φ_u and its

downstream counterpart φ_d along with the measured data. The computed surface slope determined by the proposed model is rather consistent with the measured data. As can be seen from Table 2, dam morphology is indeed affected by initial landslide velocity, valley shape and inclination of the valley bed. For instance, in rectangular valleys, the longitudinal sections of a dam are trapezoidal (low or medium initial landslide velocity) or triangular (high initial landslide velocity), and while in the forms of the other two valleys, the longitudinal section is mainly trapezoidal. When the initial landslide velocity is fixed, with an increase of valley bed inclination, the upstream surface slope decreases while the downstream counterpart increases.

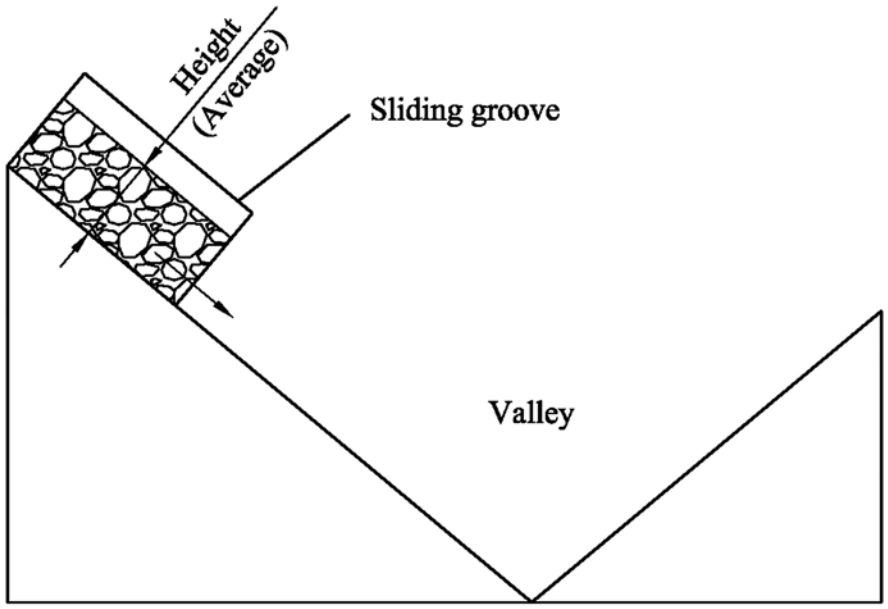

Fig. 6. Experimental setup for Series 2 (adapted from Zhao et al. [47])

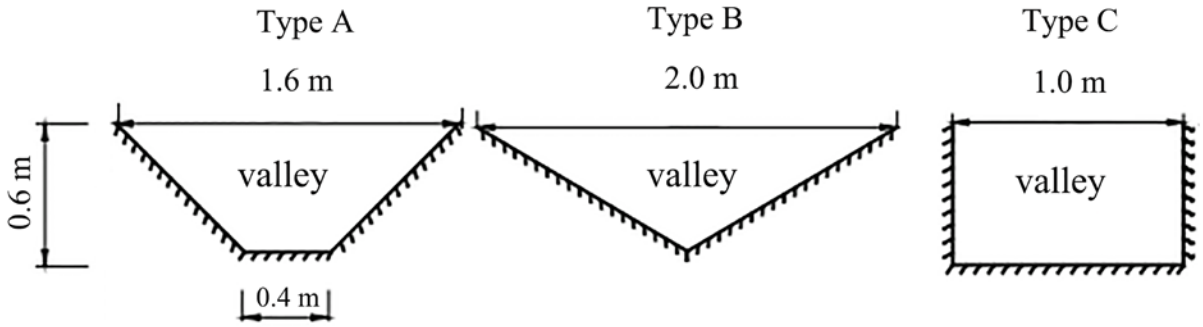

539
540 **Fig. 7.** Valley types and geometry (adapted from Zhao et al. [47]).

541

542 **Table 2** Summary of experimental landslide dam formation and results (Series 2)

Case	Valley type	Initial landslide velocity (m/s)	Froud number *Fr*	Bed inclination slope θ (°)	Measured		Computed	
					φ_u	φ_d	φ_u	φ_d
2-1	A	1	0.41	0	17	17	17.5	17.5
2-2	B	1	0.41	0	22	22	22.4	22.4
2-3	C	1	0.41	0	25	25	24.9	24.9
2-4	A	2	0.82	0	17	17	17.6	17.6
2-5	B	2	0.82	0	19	19	19.3	19.3
2-6	C	2	0.82	0	21	21	21.6	21.6
2-7	A	3	1.24	0	17	17	17.6	17.6
2-8	B	3	1.24	0	18	18	18.4	18.4
2-9	C	3	1.24	0	19	19	19.4	19.4
2-10	A	1	0.41	5	17	21	16.5	21.4
2-11	B	1	0.41	5	19	22	18.5	22.3
2-12	C	1	0.41	5	24	30	23.4	29.8
2-13	A	2	0.82	5	17	21	16.8	20.6
2-14	B	2	0.82	5	19	22	18.5	22.2
2-15	C	2	0.82	5	21	25	20.6	25.2
2-16	A	3	1.24	5	17	21	17.3	21.4
2-17	B	3	1.24	5	19	22	18.8	22.4
2-18	C	3	1.24	5	20	23	20.3	23.6
2-19	A	1	0.41	10	15	20	14.8	20.4
2-20	B	1	0.41	10	18	26	17.6	26.2
2-21	C	1	0.41	10	27	33	27.3	33.5
2-22	A	2	0.82	10	15	24	15.4	24.2
2-23	B	2	0.82	10	18	25	17.6	25.2
2-24	C	2	0.82	10	20	25	20.1	25.6
2-25	A	3	1.24	10	15	24	14.6	23.7
2-26	B	3	1.24	10	16	24	16.3	24.2
2-27	C	3	1.24	10	17	24	17.2	24.4

543

544 *3.3. Barrier lake formation due to sustained inflow of granular landslide (Series 3)*

545 This next case involves barrier lake formation due to sustained release of landslide
546 materials, which were numerically designed by Zhao et al. [29] and computed by a coupled
547 DEM-CFD model. The numerical setup comprised a grain container and an open fluid
548 channel (Fig. 8). The grain container had a size of 5 m × 5 m × 1 m, and it was placed 2 m
549 above the fluid channel. The dimension of the fluid channel was set as $L =$ 100 m, $W =$ 5
550 m, $H =$ 10 m. The computational domain included the grain container and the open fluid
551 channel. The spatial steps Δx and Δy were both 0.05 m. The discharge of granular
552 materials (q_s) into the fluid channel was kept constant. Therefore, the landslide velocity and
553 thickness were determined by the method of characteristics, while the depth-averaged
554 sediment concentration needed to be specified. Besides, a constant inflow discharge of clear
555 water was maintained throughout the simulation by setting the flow velocity at the inlet
556 boundary of the fluid channel as a constant value. At the outlet of the fluid channel, the
557 method of characteristics was used for subcritical flow conditions to obtain the updated
558 values of flow variables, which however should be set to be zero gradients for supercritical
559 flows. Within the time period considered, the fluid channel was sufficiently long to ensure
560 that the landslides did not reach the boundaries, where the boundary conditions for landslides
561 can be simply set at the initial static status. The channel's initial water depth h_{w0} was set to
562 10 m. The granular materials comprised gravel of mean diameter $d =$ 200 mm. The
563 Manning coefficients for bed roughness $n_b =$ 0.03 s/m$^{1/3}$ and interface roughness $n_w =$
564 0.005 m$^{-1/3}$ s were calibrated to the predicted results by Zhao et al. [29]. Time $t =$ 0 s

coincides with the instant that the landslide was released from the grain container. The total duration of the simulation (T_d) was 60 s.

According to grain size distribution by Zhao et al. [29], the mixture could be separated into two size fractions: d_1= 150 mm (50%) and d_2= 250 mm (50%). First, three cases with different initial flow velocities are revisited (i.e., Case 3-1, 3-2 and 3-3, see Table S1 in Supplementary materials). Then, a total of 21 numerical cases are conducted to investigate the roles of landslide inflow discharge, grain size and initial water depth (see Table S1). Specifically, landslide inflow discharge ranges from 0.5 m^3/s to 4.5 m^3/s, medium grain size varies from 10 mm to 400 mm and initial water depth increases from 5 m to 25 m. Note that in Table S1, "Y" denotes the formation of barrier lake, whilst "N" means no barrier lake is formed.

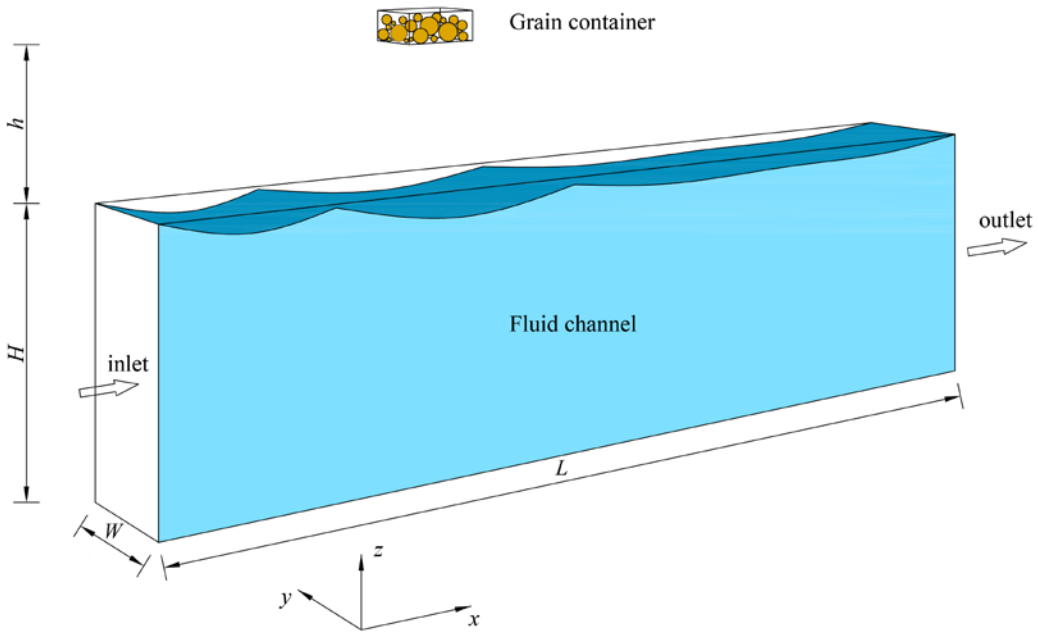

Fig. 8. Schematic view of the setup for Series 3 (modified from Zhao et al. [29]).

Figs. 9 and 10 show the computed sediment deposit lengths and heights under different initial flow velocities along with the predictions from Zhao et al. [29]. Three dimensionless number, the normalized time [T], deposit height $[\mathrm{H}]$, and length [L] are defined as $[\mathrm{T}]=t/\sqrt{h_{w0}/g}$, $[\mathrm{H}]=h/h_{w0}$ and $[\mathrm{L}]=l/L$, respectively, where the initial water depth $h_{w0}=$ 10 m and the fluid channel length $L=$ 100 m. Note that in Zhao et al. [29], the sediment deposit length was normalized by h_{w0} although the length and height did not share the same axis. Besides, the sediment deposit height is defined as the height of the static sediment layer during the simulation in Zhao et al. [29], while in the present study, it is defined as the bed aggradation depth. Due to the symmetric geometrical configuration, the deposit length is defined as the backward (for grains moving towards the inlet direction) and the forward (for grains moving towards the outlet direction) lengths of the deposit front to the symmetric axis of the grain container. In terms of deposit heights and lengths, the present model exhibits good agreement with the computed results by Zhao et al. [29]. According to Fig. 9, it is noted that for water flows with non-zero initial velocities, the forward deposit length is always larger than the backward deposit length. This is mainly because the initial flow together with the movements induced by landslides impacting into the channel can move the grains forwards along the channel. The difference between the forward and backward deposit lengths is rather large for grains transported by flows at the initial velocity of 5 m/s. For this case, the incoming grains are transported forwards by the rapid flows, such that a large number of grains can move long distances away from the source region. Fig. 10 demonstrates that the evolutions of deposit heights follow almost the same trend for these cases, and the constant height periods are evident to be observed.

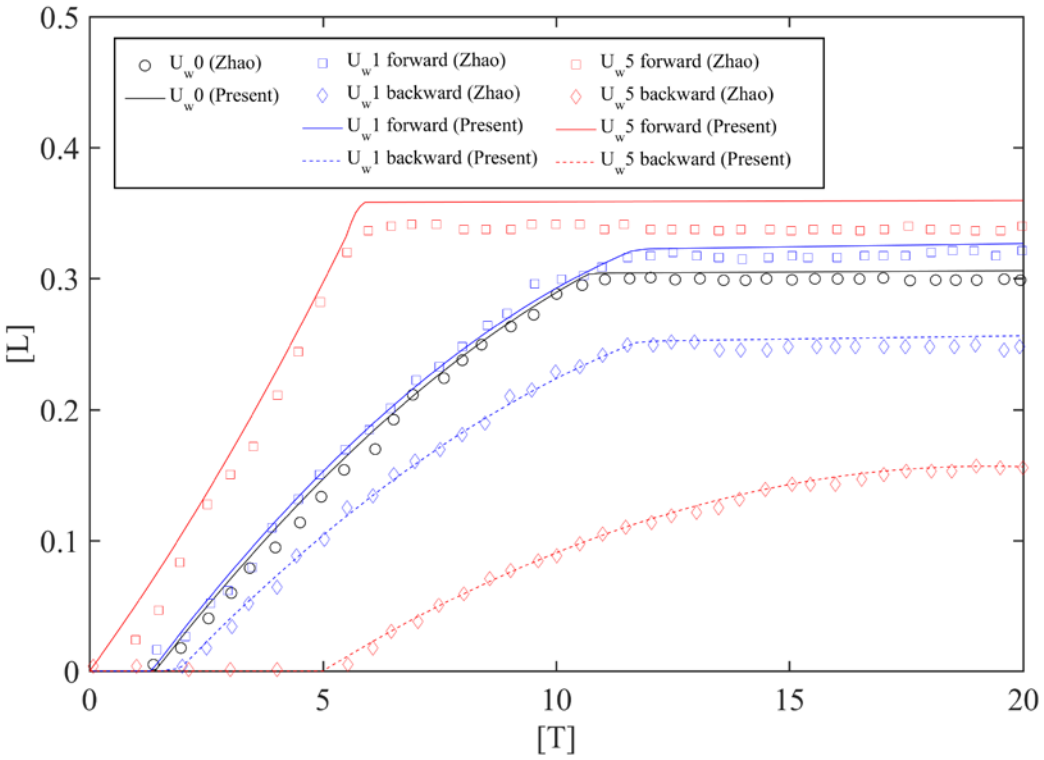

Fig. 9. Evolution of sediment deposit lengths under different initial flow velocities.

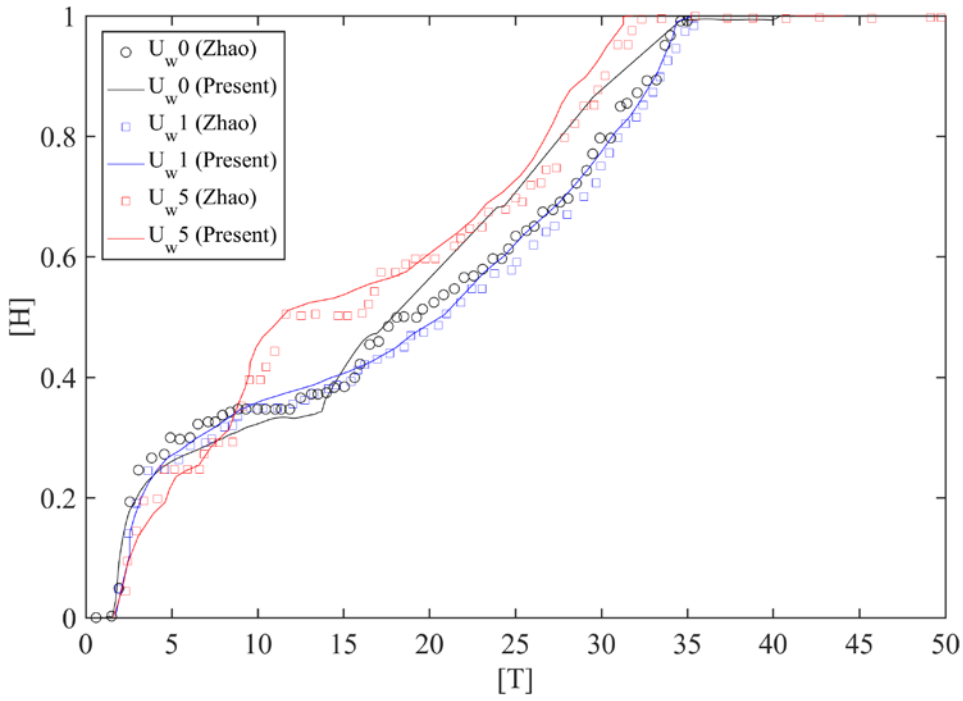

Fig. 10. Evolution of sediment deposit heights under different initial flow velocities.

608

609 Fig. 11 shows barrier lake formation process as represented by the evolutions of
610 landslide thickness plus bed deformation $h_s + \Delta z_b$ and water thickness h_w, in relation to
611 Case 3-1. Obviously, landslide directly crashes into the river and forces the water running up
612 to the opposite side of the channel. Specifically, it can be observed that solid grains move as a
613 sequence of surges. The first surge starts to spread longitudinally once the grains reach the
614 channel wall (at [T] = 2, Fig. 11a1). As evidenced by a series of successive figures, grains in
615 the first surge move with the highest mobility (see Figs. 11a1-a2) In the meantime, the
616 incoming granular grains generates the second surge spreading just on the top of the first
617 surge. The spreading velocity of the second surge is much slower than that of the first surge
618 (comparing Fig. 11a3 to Fig. 11a2). After [T] = 15, a series of small surges have formed and
619 deposited on the surface of the landslide dam. The sediments would finally block the river
620 and lead to the formation of a barrier lake after [T] = 35, when a thick and stable landslide
621 dam is formed on the river floor.

622

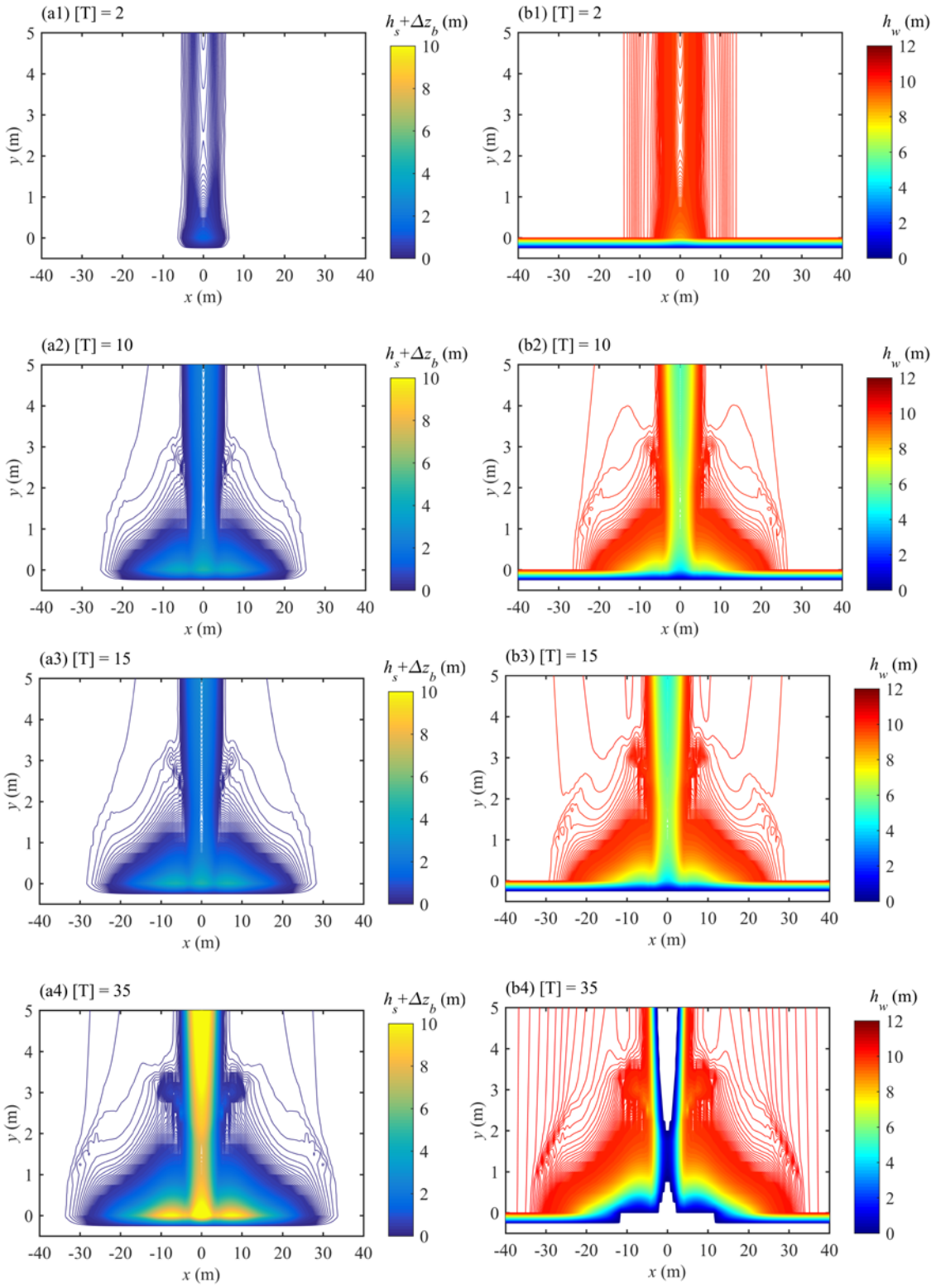

623

624 **Fig. 11.** Barrier lake formation: (a1-a4) landslide thickness plus bed deformation (b1-b4)

625 water thickness, in relation to Case 3-1.

626

3.4. Barrier lake formation due to sudden failure of granular landside (Series 4)

To further demonstrate the model performance, a total of 29 numerical cases on barrier lake formation due to sudden failure of granular landslide (Fig. 12), which was designed based on experimental landslide dam formation over dry valleys [47], are evaluated. The length of the river valley was extended to 40 m, such that the landslide would not reach the upstream and downstream boundaries of the valley within the time of computation, where the boundary conditions for landslides can be simply set at the initial static status. Similar to Series 2, the computational domain included the sliding groove and the valley. The spatial steps Δx and Δy were set as 0.02 m. First, a constant inflow discharge was maintained at the upstream of the valley to form a steady river flow, and then subaerial granular materials were released from the sliding grove. At the inlet boundary of the valley, the flow velocity and thickness were determined by the method of characteristics, while at the outlet of the fluid channel, the method of characteristics was used for subcritical flow conditions to obtain the updated values of flow variables, which however should be set to be zero gradients for supercritical flows. The roles of river flow discharge, initial landslide volume and velocity, grain size, valley type and valley bed inclination angle were investigated. Specifically, three inflow discharges were used, including 0.3 m^3/s, 0.6 m^3/s and 1.2 m^3/s. Four initial landslide volumes, i.e., 0.1 m^3, 0.2 m^3, 0.4 m^3 and 0.6 m^3, were employed to represent small, medium and large landslide. Two landslide velocities with values of 1 and 3 m/s were respectively used to represent low and fast landslide movements. Following Zhao et al. [47], the valley shape was set to be rectangular, trapezoidal or V-shaped to investigate the influence of valley shape (see Fig. 2). Two values, i.e., 0° and 5°, were selected to represent the flat and sloping

valley bed. Table S2 in Supplementary materials summarizes the initial conditions of these numerical cases and the results. Notably, it is impossible to form the landslide dam in case of the river low with high velocity (i.e., the upstream river flow discharge is equal to 1.2 m^3/s). In general, smaller river flow discharge, larger landslide volume and velocity, coarser grain size, milder valley bed inclination angle, and rectangular valley shape are conducive to barrier lake formation. Fig. 13, Fig. 14 and Video S1 in Supplementary materials collectively show barrier lake formation due to sudden failure of the landslide, in relation to Case 4-1. During the first stage, the landslide impacts into the channel and interacts with the river flow. Due to the low velocity of the river flow, the front landslide can even climb to the other side of the channel (Fig. 13a1 and Fig. 14a). Later, most of the landslide materials are deposited on the channel bottom, forming the landslide dam (Fig. 13a2 and Fig. 14b). Soon after the dam formation, the barrier lake is formed due to the blockage (Fig. 13b3 and Fig. 14c), and the volume of the barrier lake gradually increases due to sustained upstream inflow, as shown in Fig. 13b4 and Figs. 14d-f. With the increase of the lake volume, the water level exceeds the dam height, overtopping begins (see Video S1, $t >$ 54 s).

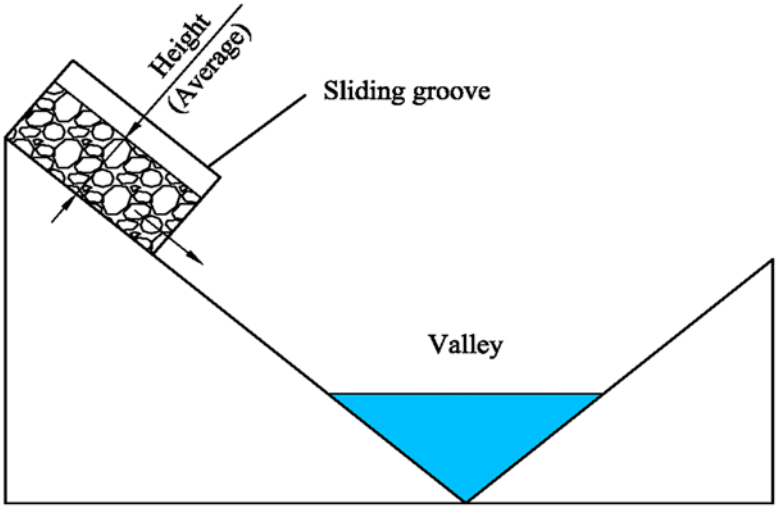

Fig. 12. Numerical setup for Series 4 (modified from Zhao et al. [47]).

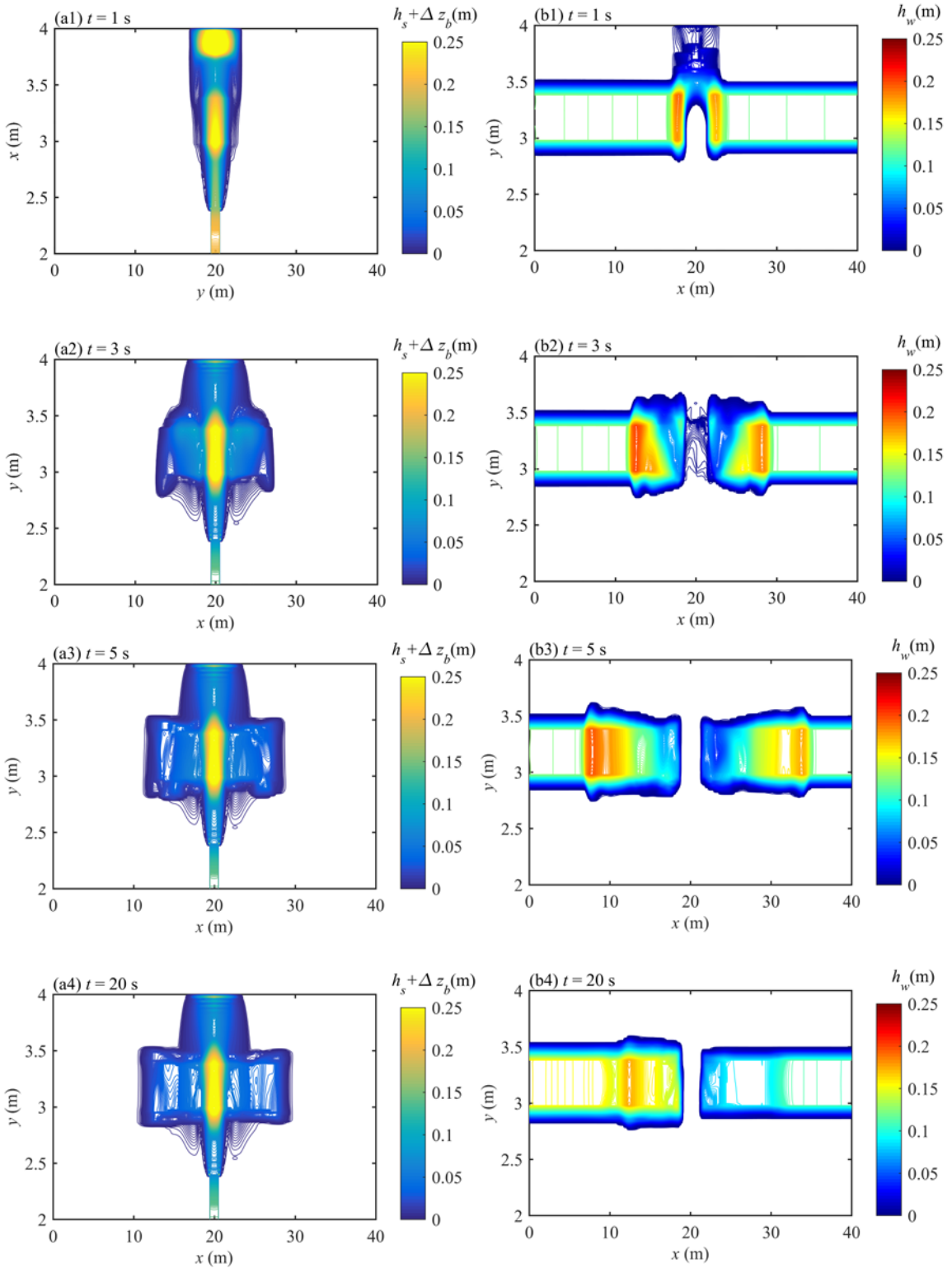

669

670 **Fig. 13.** Barrier lake formation in relation to Case 4-1: (a1-a4) landslide thickness plus bed

671 deformation (b1-b4) water thickness.

672

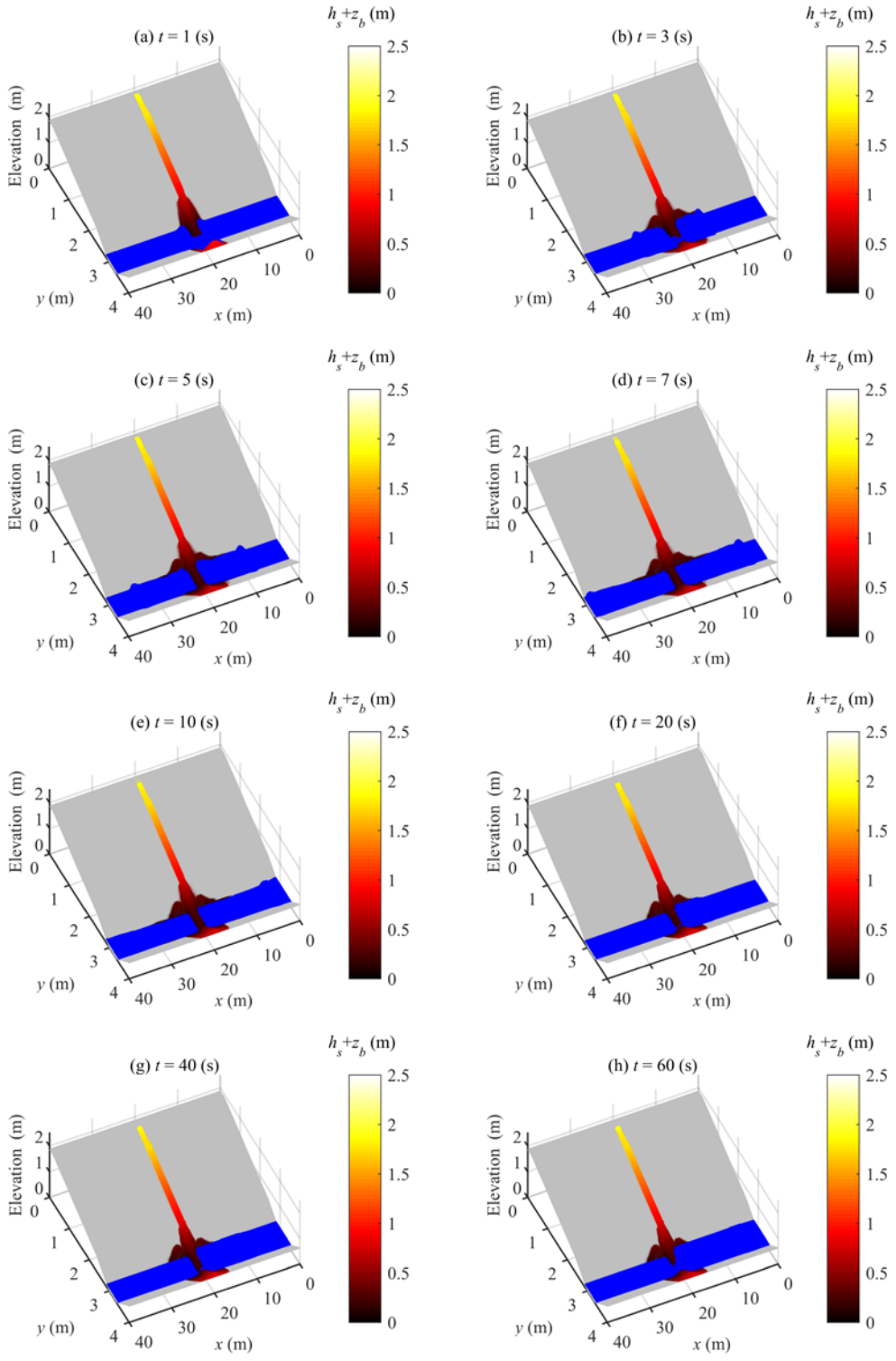

Fig. 14. Typical instants of barrier lake formation in relation to Case 4-1.

Overall, the present double layer-averaged two-phase flow model has satisfactorily

678 resolved barrier lake formation due to landslide impacting a river (Sections 3.3 and 3.4).
679 Nevertheless, it may not necessarily mean the present model would be universally valid as
680 the numerical case studies were conducted in flumes with fixed bed slopes. In this connection,
681 more large-scale experiments on barrier lake formation with varied flume beds and more
682 observed data on natural barrier lake over irregular and steep slopes are warranted to further
683 support model development.

684

685 **4. Discussion**

686 *4.1. Interphase interactions*

687 It evaluates the interphase interactions by virtue of the relative velocities. Physically,
688 interphase interactions quantify the momentum and energy transfer between grains and fluids
689 [76], which essentially characterize waves and sediment transport due to granular landslides
690 impacting water bodies [77-78]. However, these processes have not yet been sufficiently
691 resolved as existing continuum models involve a single-phase flow assumption and presume
692 a single sediment size and discrete models cannot fully account for sediment transport. Here
693 V_{fs} and U_{fs} are defined as the velocity differences between the water phase of landslide
694 and the sediment phase of any size in the transverse ($y-$axis) and longitudinal ($x-$axis)
695 directions, respectively. Accordingly, $V_{fs}=v_f - v_{sk}$ and $U_{fs}=U_f - U_{sk}$, both of which are
696 normalized by $\sqrt{gh_{w0}}$. Therefore, $[V_{fs}]=V_{fs}\big/\sqrt{gh_{w0}}$ and $[U_{fs}]=U_{sf}\big/\sqrt{gh_{w0}}$. In relation to
697 Case 3-1, Fig. 15 displays the velocity differences between the water and size-specific
698 sediment phases of landslide in the transverse ($y-$axis) direction, while Fig. 16 shows the

699 counterparts in the longitudinal ($x-$ axis) direction.

700 As seen in Figs. 15, before reaching the channel wall at $y=0$ m, the grains generally
701 have higher speeds than the water phase in the transverse direction ($y-$ axis), while the
702 coarse grains move faster than the fine grains by approximately 20% - 30%. After hitting the
703 wall, the landslide spread longitudinally and its velocity decreases. Compared to the water
704 phase, the grains decelerate more rapidly and move slower at the area around the wall,
705 although they still sustain a higher speed than the water on the edge of this area. Note that the
706 coarse grains settle faster than the fine grains as a larger grain size corresponds to a larger
707 absolute velocity difference in the transverse direction. Later, it is shown in Figs. 15(a3-a4)
708 and Figs. 15(b3-b4) that the velocity differences between the water and sediment phases
709 gradually shrink. This occurs because the barrier lake gradually forms (as shown in Fig. 11),
710 which greatly impedes the subsequent impact of landslide into the river.

711 Regarding the normalized velocity differences in the longitudinal direction ($x-$ axis),
712 $U_{fs}>0$ in the downstream direction and $U_{fs}<0$ in the upstream direction indicate a
713 higher water speed than the sediment phases, and vice versa. As shown in Fig. 16, it is
714 observed that $U_{fs}>0$ where $x>0$, while $U_{fs}<0$ where $x<0$. Therefore, the grains
715 generally exhibit lower speeds than the water, though only a marginal velocity difference can
716 be distinguished. In contrast to the observations in the transverse direction, the coarse grains
717 move slightly slower than the fine grains. As time is going on (see Figs. 16 a3-a4 and Figs. 16
718 b3-b4), the presence of the barrier lake tends to dampen the velocity differences between the
719 water and sediment phases in the longitudinal direction, similar to those observed in the
720 transverse direction (Figs. 15 a3-a4 and Figs. 15 b3-b4).

721 Figs. 15 and 16 collectively show that water and grain velocities are disparate, which
722 characterize the primary role of grains in driving water movement in subaqueous landslide
723 motion. Consequently, grains play a major role in barrier lake formation due to granular
724 landslide impacting a river. Overall, these results clearly imply that a double layer-averaged
725 two-phase flow model is warranted, physically characterizing a step forward for barrier lake
726 formation as compared with a double layer-averaged single-phase flow model [22], in which
727 sediment velocity is assumed to be equal to that of the fluid phase.
728

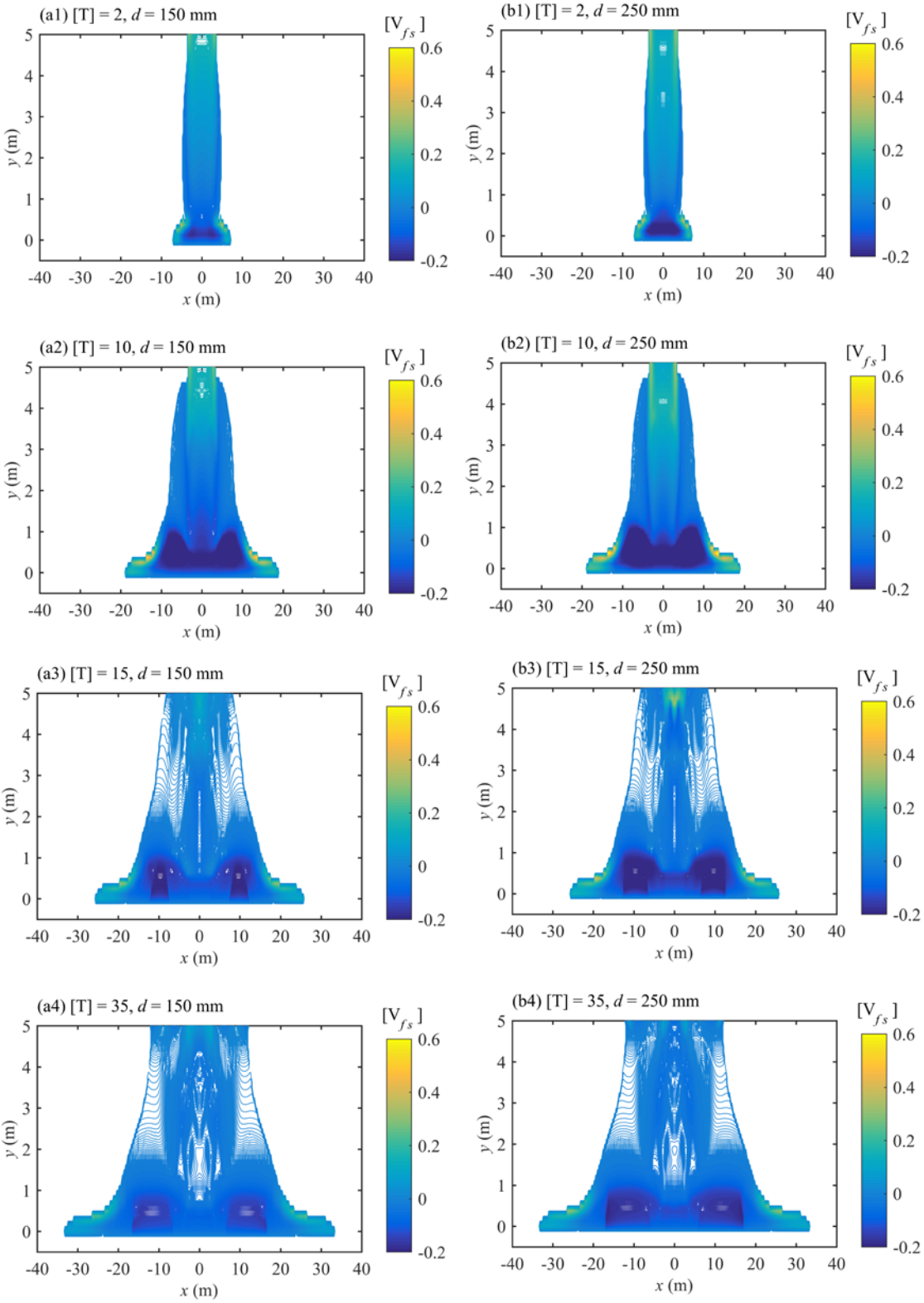

729

730 **Fig. 15.** Velocity differences between the water and sediment phases of landslide in

731 transverse (y – axis) direction, in relation to Case 3-1, a1-a4 with $d =$ 150 mm, and b1-b4

732 with $d =$ 250 mm.

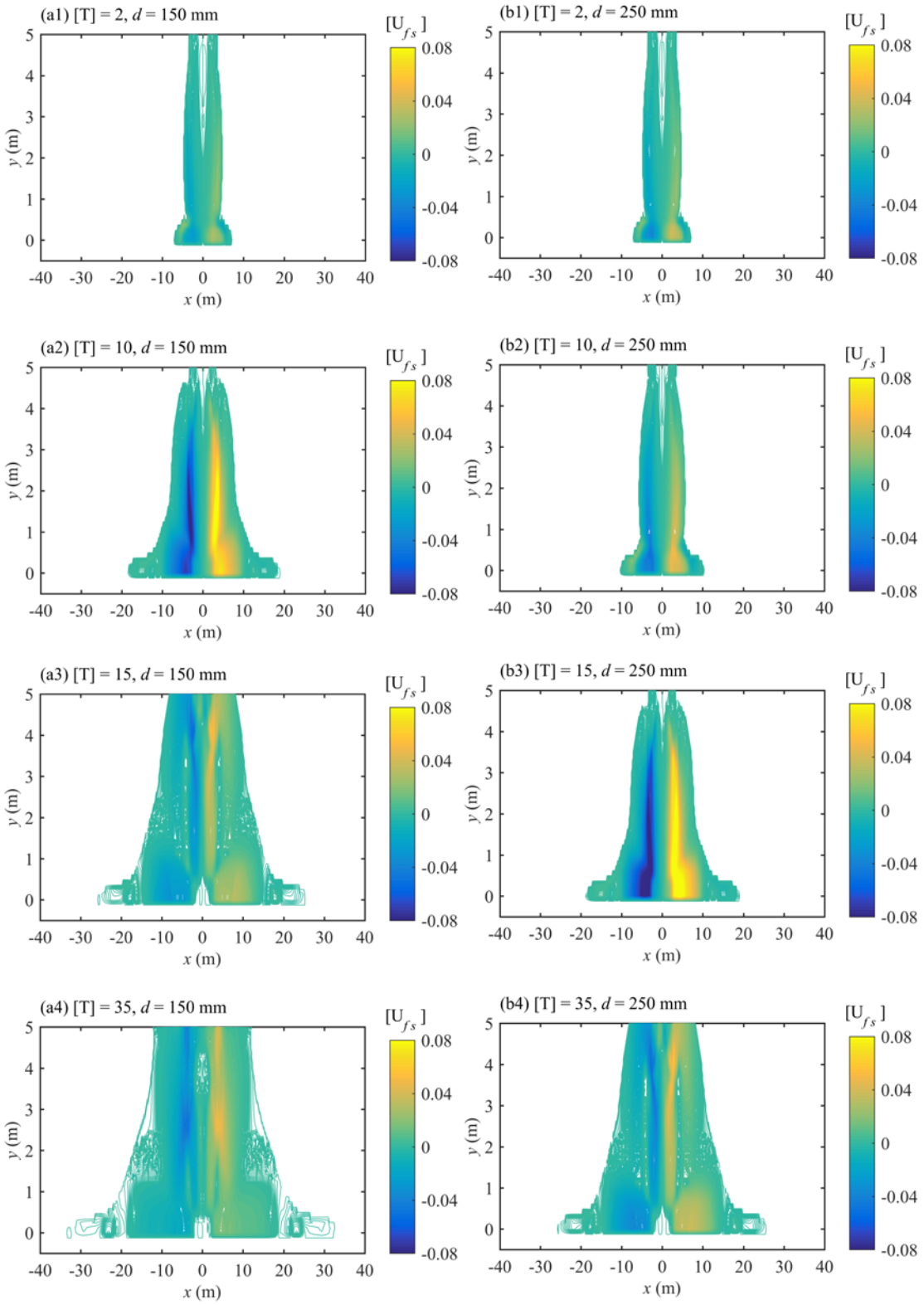

733

734 **Fig. 16.** Velocity differences between the water and sediment phases of landslide in

735 longitudinal (x – axis) direction, in relation to Case 3-1,a1-a4 with $d =$ 150 mm, b1-b4 with

736 $d =$ 250 mm.

4.2. Grain size effects

In section 3, the proposed model has demonstrated its capability of reproducing barrier lake formation due to landslide impacting a river, in addition to resolving the effects of critical factors, including initial landslide velocity, river flow condition, valley type, and bed inclination angle. However, to date, there is a lack of studies available for investigating grain size effects on barrier lake formation process, although grain sizes and grain-size heterogeneity have been known as two of the most important factors controlling the characteristics of landslide dams [37]. This is mainly because sediment transport has not been fully accounted for by previous models.

4.2.1. Coarse vs Fine grain size

As stated above, discrete models [29-30, 32-33] generally exclude fine grains to improve computational efficiency. Such practices are certainly far from justified as coarse grains can be deposited faster than finer grains under a given flow condition. Here, in relation to Cases 3-8, 3-9 and 3-10, three different sediment mixtures with smaller mean diameters, i.e., d_m = 100 mm, 50 mm and 10 mm, are used for analysis. Evolutions of sediment deposit heights under different mean diameters are presented in Fig. 17. Obviously, the computed results are rather sensitive to the grain size. The larger the grain size, the faster the barrier lake can be formed. Notably, when the grain size is rather small (i.e., $d_m <$ 50 mm), the barrier lake cannot be formed within the considered computational time.

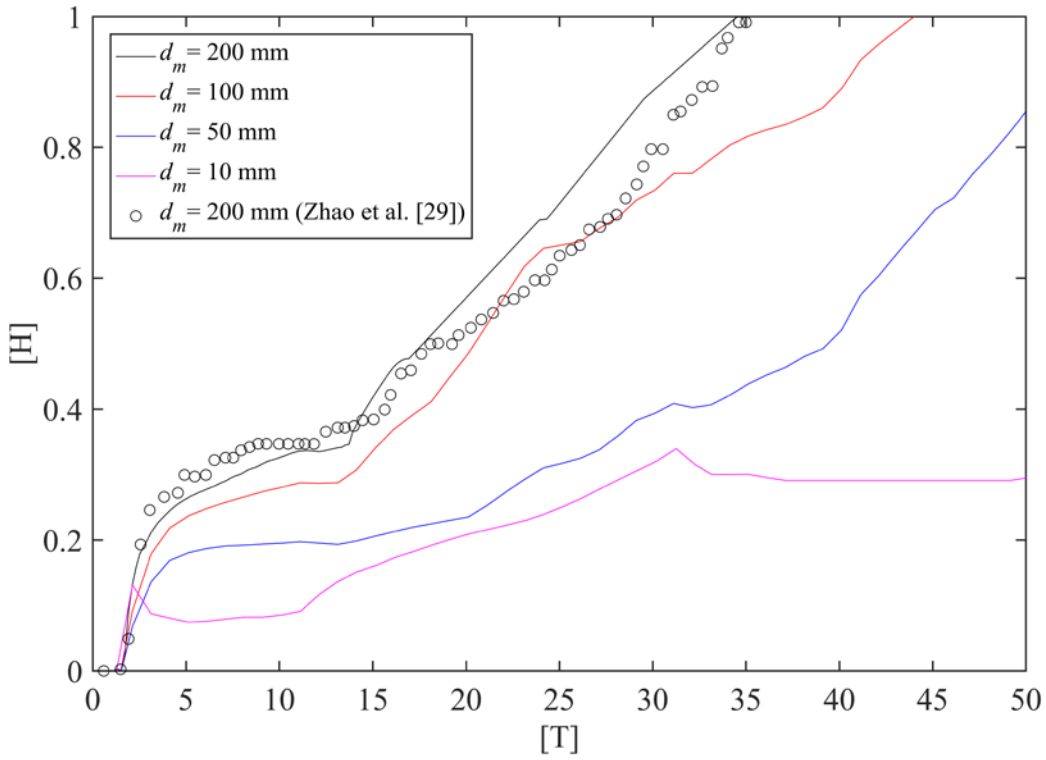

Fig. 17. Evolution of sediment deposit heights under different mean diameters.

4.2.2. Broad vs Narrow grain size distribution

Another shortcoming in existing models is that multi grain sizes are not sufficiently incorporated. Specifically, DEM-CFD models [29] usually assume much narrower grain size distributions than the real cases to reduce computational costs, while the double layer-averaged single-phase flow model [22], MPM two-phase models [27], SPH models [28] and DDA-SPH models [32-33] presume a single sediment size. Clearly, these practices cannot reflect the nature of sediment compositions in landslides, fundamentally featured by the broadly distributed grain sizes, ranging from clay size ($\approx 10^{-5}$ m) to boulder size ($\approx 10^{1}$ m) [36]. To address the effect of the grain size distribution (GSD), the grain-size heterogeneity is

771 adjusted by increasing the standard deviation of sediment composition (i.e., σ was
772 increased from 1.29 to 2.88), while retaining the same mean sediment diameter ($d_m =$ 200
773 mm) (Table 3). Fig. 18 illustrates the evolutions of sediment deposit heights under two GSDs,
774 in relation to Case 3-1. The sediment deposit height under a broader GSD increases much
775 slower than its counterpart with a much narrower GSD. And within the considered
776 computational time, the river is not blocked by the landslide and no barrier lake is formed
777 (Fig. 19). By comparing Fig. 19 to Fig. 11, it is found that the landslide with a higher
778 grain-size heterogeneity spreads faster and further after entering into the flume, echoing the
779 previous finding that grain-size heterogeneity can enhance landslide mobility [79].

780 Overall, the analysis above (Sections 4.2.1 and 4.2.2) clearly demonstrate that coarse
781 grains and grain-size uniformity favour barrier lake formation. Furthermore, it is implied that
782 existing discrete models [27-29, 32-33] exclude fine grains and presume narrower grain size
783 distributions or a single sediment size and the double layer-averaged single-phase flow model
784 [22] that assumes a single sediment size are inadequate for barrier lake formation due to
785 granular landslide impacting a river.

786

Table 3 Grain size distribution

Broad GSD: d_m = 200 mm, σ = 2.88				
d_i (mm)	20	120	200	500
(%)	20	30	30	20
Narrow GSD: d_m = 200 mm, σ = 1.29				
d_i (mm)	150		250	
(%)	50		50	

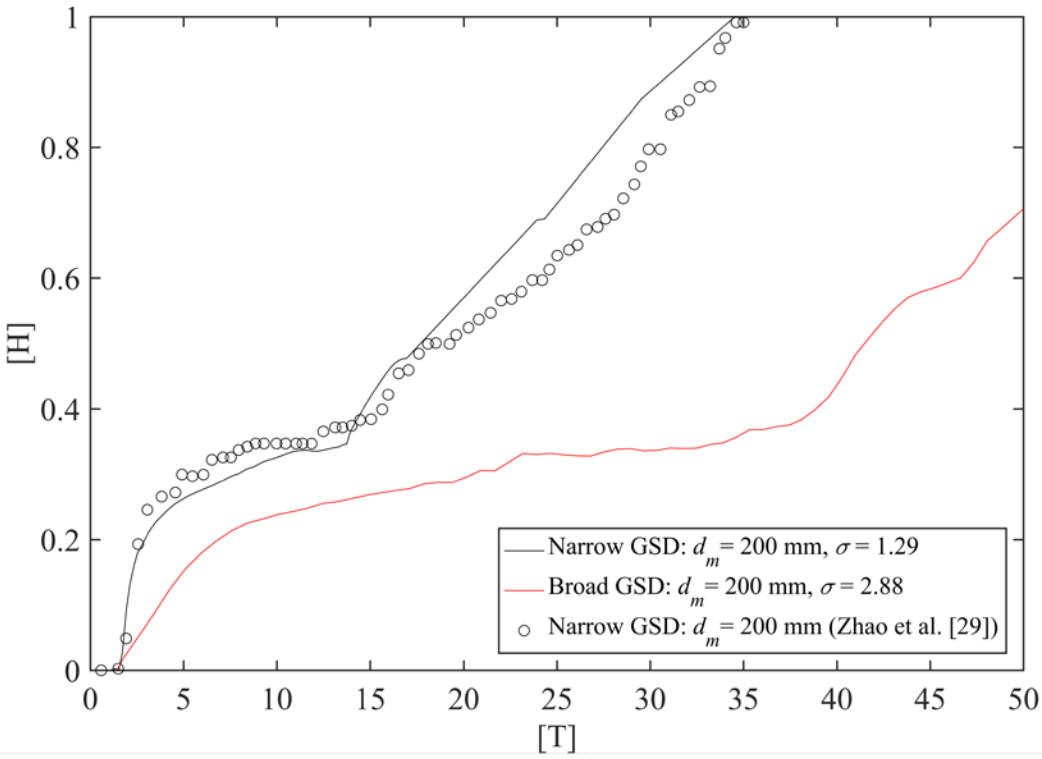

Fig. 18. Evolutions of sediment deposit heights under different grain size distributions, in relation to Case 3-1.

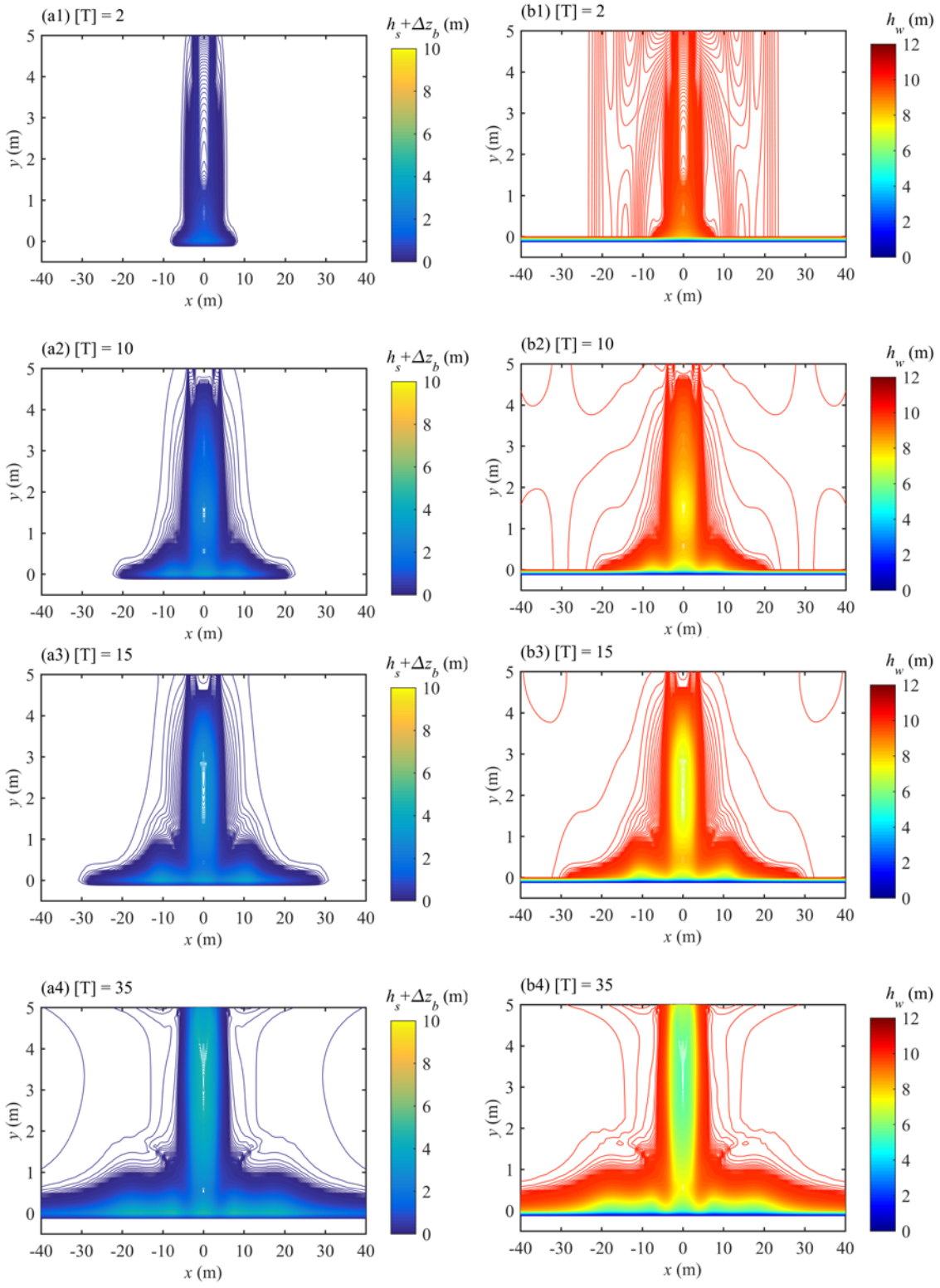

794

795 **Fig. 19.** Landslide movements and waves under a broad grain size distribution, in relation to

796 Case 3-1: (a1-a4) landslide thickness plus bed deformation (b1-b4) water thickness.

797

798 *4.3. Threshold for barrier lake formation*

799 The possibility that a barrier lake can be formed depends on many geomorphic factors
800 that concurrently involve both landslide and river dynamics [80]. Accordingly, the critical
801 index for barrier lake formation can be formulated by incorporating geomorphic variables of
802 both river and landslide. Existing critical indexes mainly include Annual Constriction Ratio
803 (ACR, Swanson et al. [81]), Dimensionless Flow Index (DFI, Ermini and Casagli [4]),
804 Dimensionless Constriction Index (DCI, Ermini and Casagli [4]), Dimensionless
805 Morpho-Invasion Index (DMI, Dal Sasso et al. [80]) and Morphological Obstruction Index
806 (MOI, Stefanelli et al. [82]). Specifically, ACR is defined as the ratio of the river channel
807 width to the landslide velocity. DFI is correlated with the landslide mass and the river
808 discharge, while DCI accounts for the grain size of landslide material based on DFI. MOI is
809 defined as the ratio of the landslide mass to the river channel width. Comparatively, DMI is
810 determined by the landslide-to-river momentum ratio. As compared to other indexes, DMI is
811 physically enhanced by incorporating the geometric, kinematic and dynamic characteristics
812 of landslide and river systems simultaneously [80]. However, DMI neglects the effect of
813 grain size, the role of which on barrier lake formation is demonstrated to be significant (see
814 Section 4.2).

815 In this study, a new non-dimensional critical index is proposed, which is defined as
816 follows,

817 $$I_{MP} = R_V R_u R_\rho / \theta \tag{15}$$

818 where R_V is the volume ratio of the landslide to the river and defined as $R_V = V_s / bh_{w0}^2$;

819 $R_u = U_s / U_w$ is the velocity ratio of the landslide to the river flow; $R_\rho = \rho_m / \rho_w$ is the
820 density ratio of the landslide to the river flow; θ is the Shields number. For the cases due to
821 sustained inflow of landslide material (i.e., Series 3), $V_s = q_s T_d$, while for the cases due to
822 sudden failure of landslide (i.e., Series 4), V_s is the initial landslide volume. Moreover, U_s
823 is the initial landslide velocity and U_w is equal to the initial river flow velocity. ρ_m is
824 equivalent to the initial landslide density. Physically, $R_m = R_V R_u R_\rho$ represents the
825 momentum ratio of the landslide to the river flow. Shields number θ characterizes the
826 mobility of sediment, which generally increases along with the decrease of grain size under a
827 given condition. Therefore, the proposed critical index I_{MP} accounts for both
828 landslide-to-river momentum ratio and grain size effect.

829 Table S3 in Supplementary materials summarizes the computed critical index I_{MP} for
830 Series 3 and 4. Fig. 20 presents the computed $R_V R_\rho / \theta$ against the velocity ratio R_u along
831 with solid circle and open square symbols respectively indicating barrier lake is formed and
832 not-formed. Importantly, the formation of a barrier lake occurs when $I_{MP} >$ 0.836;
833 otherwise, barrier lake cannot be formed. In general, barrier lake formation is more likely to
834 occur with the increase of both landslide-to-river momentum ratio and grain size.

835

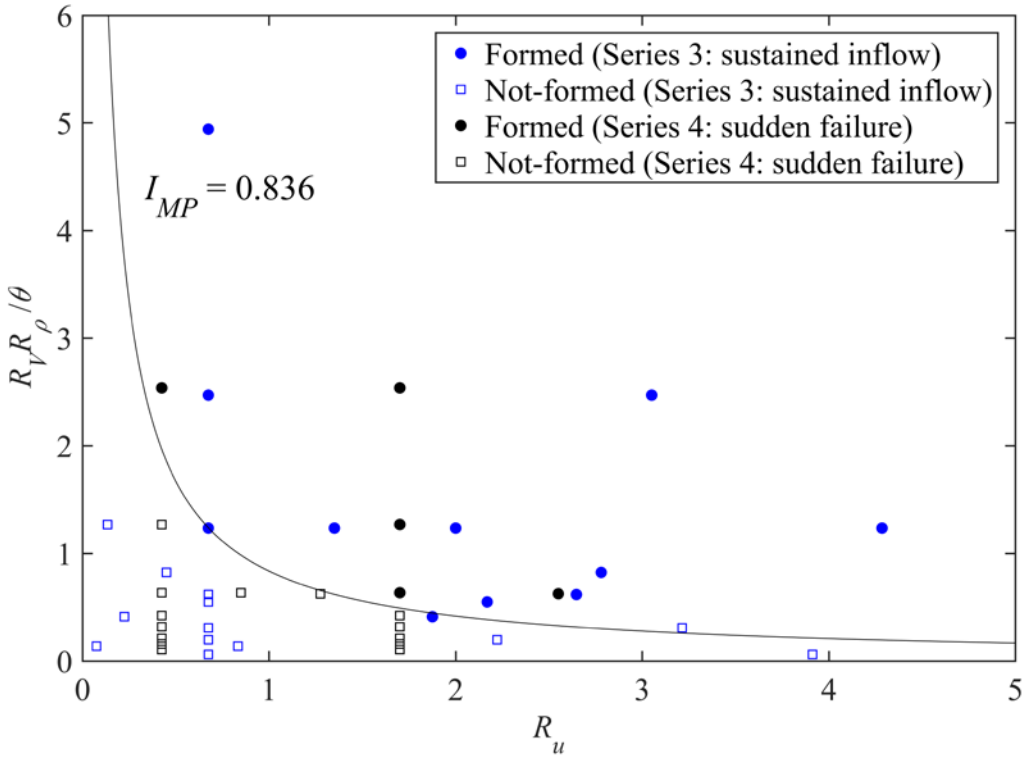

836

837 **Fig.20.** Threshold for barrier lake formation as presented by computed $R_V R_\rho / \theta$ against the

838 velocity ratio R_u along with solid circle and open square symbols respectively showing

839 barrier lake is formed and not-formed.

840

841 **5. Conclusions**

842 A new double layer-averaged two-phase flow model is presented and applied to solve

843 barrier lake formation due to landslide impacting a river. Physically, it represents a step

844 forward compared with existing models based on discrete or continuum assumption, which

845 cannot fully resolve sediment transport (Table 1). The main conclusions are as follows:

846 1. The proposed model is validated by the benchmark laboratory experiments of waves

847 due to landslides impacting reservoirs and landslide dam formation over dry valleys. It

848 reasonably resolves barrier lake formation for extended numerical case studies, as per the

849 effects of key factors, including initial landslide volume and velocity, grain size, river flow
850 condition, valley type, and valley bed inclination angle.

851 2. It is shown that grains essentially drive the water movement in subaqueous landslide
852 motion and thus significantly affect barrier lake formation afterwards. Equally importantly,
853 coarse grains and grain-size uniformity favour barrier lake formation. These results underpin
854 that numerical continuum models, which involve a single-phase flow assumption and
855 presume a single-sized sediment, and discrete models, which preclude fine grains and assume
856 narrow grain size distributions or a single sediment size, are inadequate for barrier lake
857 formation.

858 3. A new non-dimensional threshold for barrier lake formation is proposed, based on
859 landslide-to-river momentum ratio and grain size. It is implied that a barrier lake is more
860 likely to form with the increase of both landslide-to-river momentum ratio and grain size.
861 This approach can serve as a useful tool in decision-making associated with prediction of
862 barrier lake formation and management of emergencies induced by these events.

863 The present work facilitates a promising modelling framework for barrier lake formation
864 due to granular landslide impacting a river, and therefore enhances whole-process flood risk
865 management due to barrier lakes when coupled with the recent models for barrier lake failure
866 and the resulting floods. Inevitably, uncertainties of the proposed model arise from the
867 estimations of mass exchange between the landslide and the bed, interface and bed
868 resistances, which require systematic fundamental investigations into the associated
869 mechanisms.

870

871 **Acknowledgements**

872 This research was funded by the Natural Science Foundation of China under Grants No.
873 11672212 and 11432015.

874

875 **References**

876 [1] J.E. Costa, R.L. Schuster, The formation and failure of natural dams, Geol. Soc. Am. Bull.
877 100 (1988) 1054–1068.
878 https://doi.org/10.1130/0016-7606(1988)100<1054:TFAFON>2.3.CO;2.
879 [2] T.W. Van Asch, J. Buma, L.P.H. Van Beek, A view on some hydrological triggering
880 systems in landslides, Geomorphology 30 (1999) 25-32.
881 https://doi.org/10.1016/S0169-555X(99)00042-2
882 [3] X. Fan, Q. Xu, A. Alonso-Rodriguez, et al., Successive landsliding and damming of the
883 Jinsha River in eastern Tibet, China: prime investigation, early warning, and emergency
884 response, Landslides 16 (2019) 1003-1020.
885 https://doi.org/10.1007/s10346-019-01159-x.
886 [4] L. Ermini, N. Casagli, Prediction of the behavior of landslide dams using a geomorphical
887 dimensionless index, Earth Surf. Process Landf. 28 (2003) 31-47.
888 https://doi.org/10.1002/esp.424.
889 [5] Y. Shang, Z. Yang, L. Li, D.A. Liu, Q. Liao, Y. Wang, A super-large landslide in Tibet in
890 2000: background, occurrence, disaster, and origin, Geomorphology 54 (2003) 225-243.
891 https://doi.org/10.1016/S0169-555X(02)00358-6.
892 [6] F.C. Dai, C.F. Lee, J.H. Deng, L.G. Tham, The 1786 earthquake-triggered landslide dam
893 and subsequent dam-break flood on the Dadu River, southwestern China,
894 Geomorphology 65 (2005) 205-221. https://doi.org/10.1016/j.geomorph.2004.08.011.
895 [7] T.Y. Duman, The largest landslide dam in turkey: Tortum landslide, Eng. Geol. 104
896 (2009) 66-79. http://dx.doi.org/10.1016/j.enggeo.2008.08.006.
897 [8] Q. Xu, X.M. Fan, R.Q. Huang, C. Westen, Landslide dams triggered by the Wenchuan

Earthquake, Sichuan Province, south west China, Bull. Eng. Geol. Environ. 68 (2009) 373–386. https://doi.org/10.1007/s10064-009-0214-1

[9] J.W. Zhou, P. Cui, H. Fang, Dynamic process analysis for the formation of Yangjiagou landslide-dammed lake triggered by the Wenchuan earthquake, China, Landslides 10 (2013) 331–342. https://doi.org/10.1007/s10346-013-0387-3.

[10] Z. Cao, Z. Yue, G. Pender, Landslide dam failure and flood hydraulics. Part I: experimental investigation, Nat. Hazards 59 (2011) 1003-1019. https://doi.org/10.1007/s11069-011-9814-8.

[11] Kakinuma, T., Shimizu, Y., 2014. Large-scale experiment and numerical modeling of a riverine levee breach, J. Hydraul. Eng. 140, 04014039. https://doi.org/10.1061/(ASCE)HY.1943-7900.0000902.

[12] I. Rifai, K. El Kadi Abderrezzak, S. Erpicum, P. Archambeau, D. Violeau, M. Pirotton, B. Dewals, Floodplain backwater effect on overtopping induced fluvial dike failure, Water Resour. Res. 54 (2018) 9060-9073. https://doi.org/10.1029/2017WR022492.

[13] R. Faeh, Numerical modeling of breach erosion of river embankments, J. Hydraul. Eng. 133 (2007) 1000-1009. https://doi.org/10.1061/(ASCE)0733-9429(2007)133:9(1000).

[14] Z. Cao, Z. Yue, G. Pender, Landslide dam failure and flood hydraulics. Part II: coupled mathematical modelling, Nat. Hazards 59 (2011)1021-1045. https://doi.org/10.1007/s11069-011-9815-7.

[15] Z. Cao, Z. Yue, G. Pender, Flood hydraulics due to cascade landslide dam failure, J. Flood Risk Manag. 4 (2011) 104-114. https://doi.org/10.1111/j.1753-318X.2011.01098.x.

[16] W. Wu, R. Marsooli, Z. He, Depth-averaged two-dimensional model of unsteady flow and sediment transport due to noncohesive embankment break/breaching, J. Hydraul. Eng. 138 (2011) 503-516. https://doi.org/10.1029/2017WR022492.

[17] Chen, Z., Ma, L., Yu, S., Chen, S., Zhou, X., Sun, P., Li, X., 2015. Back analysis of the draining process of the Tangjiashan barrier lake. J. Hydraul. Eng. 141(4), 05014011. https://doi.org/10.1061/(ASCE)HY.1943-7900.0000965.

[18] H. Ma, X. Fu, Real time prediction approach for floods caused by failure of natural dams due to overtopping, Adv. Water Resour. 35 (2012) 10-19.

928 https://doi.org/10.1016/j.advwatres.2011.08.013.
929 [19] H.M. Fritz, W.H. Hager, H.E. Minor, Near field characteristics of landslide generated
930 impulse waves, J. Waterw. Port. C. 130 (2004), 287-302.
931 https://doi.org/10.1061/(ASCE)0733-950X(2004)130:6(287)
932 [20] V. Heller, W.H. Hager, Wave types of landslide generated impulse waves, Ocean Eng. 38
933 (2011) 630-640. https://doi.org/10.1016/j.oceaneng.2010.12.010.
934 [21] F. Bregoli, A. Bateman, V. Medina, Tsunamis generated by fast granular landslides: 3D
935 experiments and empirical predictors, J. Hydraul. Res. 55 (2017) 743-758.
936 https://doi.org/10.1080/00221686.2017.1289259.
937 [22] J. Li, Z. Cao, Q. Liu, Waves and sediment transport due to granular landslides impacting
938 reservoirs, Water Resour. Res. 55 (2019) 495-518.
939 https://doi.org/:10.1029/2018WR023191.
940 [23] Cao, Z., Xia, C., Pender, G., Liu, Q., 2017. Shallow water
941 hydro-sediment-morphodynamic equations for fluvial processes. J. Hydraul. Eng. 143(5),
942 02517001 (Forum Article). http://dx.doi.org/10.1061/(ASCE)HY.1943-7900.0001281.
943 [24] Y. Cui, A. Nouri, D. Chan, E. Rahmati, A new approach to DEM simulation of sand
944 production, J. Petrol Sci. Eng. 147 (2016), 56-67.
945 https://doi.org/10.1016/j.petrol.2016.05.007
946 [25] W. Wang, H. Zhang, L. Zheng, Y.B. Zhang, Y.Q. Wu, S.G. Liu, A new approach for
947 modeling landslide movement over 3D topography using 3D discontinuous deformation
948 analysis, Comput. Geotech. 81 (2017) 87-97.
949 https://doi.org/10.1016/j.compgeo.2016.07.015
950 [26] L. Cascini, S. Cuomo, M. Pastor, G. Sorbino, L. Piciullo, SPH run-out modelling of
951 channelised landslides of the flow type, Geomorphology 214 (2014) 502-513.
952 https://doi.org/10.1016/j.geomorph.2014.02.031
953 [27] S. Bandara, K. Soga, Coupling of soil deformation and pore fluid flow using material
954 point method, Comput. Geotech. 63 (2015) 199-214.
955 https://doi.org/10.1016/j.compgeo.2014.09.009
956 [28] C. Shi, Y. An, Q. Wu, Q. Liu, Z. Cao, Numerical simulation of landslide-generated
957 waves using a soil-water coupling smoothed particle hydrodynamics model. Adv. Water

958 Resour. 92 (2016) 130-141. https://doi.org/10.1016/j.advwatres.2016.04.002
959 [29] T. Zhao, F. Dai, N.W. Xu, Coupled DEM-CFD investigation on the formation of
960 landslide dams in narrow rivers, Landslides 14 (2017) 189-201.
961 https://doi.org/10.1007/s10346-015-0675-1.
962 [30] W.J. Xu, Z.G. Yao, Y.T. Luo, X.Y. Dong, Study on landslide-induced wave disasters
963 using a 3D coupled SPH-DEM method, Bull. Eng. Geol. Environ. in press (2019).
964 https://doi.org/10.1007/s10064-019-01558-3
965 [31] A. Leonardi, F.K. Wittel, M. Mendoza, R. Vetter, H.J. Herrmann,
966 Particle–fluid–structure interaction for debris flow impact on flexible barriers, Comput.
967 Aided Civ. Inf. 31 (2016) 323-333. https://doi.org/10.1111/mice.12165
968 [32] W. Wang, G. Chen, Y. Zhang, L. Zheng, H. Zhang, Dynamic simulation of landslide dam
969 behavior considering kinematic characteristics using a coupled DDA-SPH method, Eng.
970 Anal. Bound. Elem. 80 (2017) 172-183.
971 https://doi.org/10.1016/j.enganabound.2017.02.016.
972 [33] W. Wang, K. Yin, G. Chen, B. Chai, Z. Han, J. Zhou, Practical application of the coupled
973 DDA-SPH method in dynamic modeling for the formation of landslide dam, Landslides
974 16 (2019) 1021-1032. https://doi.org/10.1007/s10346-019-01143-5.
975 [34] M. Sakai, H. Takahashi, C.C. Pain, J.P. Latham, J. Xiang, Study on a large-scale discrete
976 element model for fine particles in a fluidized bed, Adv. Powder Technol. 23 (2012)
977 673–681. https://doi.org/10.1016/j.apt.2011.08.006.
978 [35] T. Zhao, G.T. Houlsby, S. Utili, Investigation of granular batch sedimentation via
979 DEM–CFD coupling, Granular Matter 16 (2014) 921-932.
980 https://doi.org/10.1007/s10035-014-0534-0.
981 [36] D.S. Chang, L.M. Zhang, Simulation of the erosion process of landslide dams due to
982 overtopping considering variations in soil erodibility along depth, NHESS 10 (2010)
983 933–946. https://doi.org/10.5194/nhess-10-933-2010.
984 [37] R. Kaitna, M.C. Palucis, B. Yohannes, K.M. Hill, W.E. Dietrich, Effects of coarse grain
985 size distribution and fine particle content on pore fluid pressure and shear behavior in
986 experimental debris flows, J. Geophys. Res.- Earth Surf. 121 (2016) 415-441.
987 https://doi.org/10.1002/2015JF003725

[38] N. Casagli, L. Ermini, G. Rosati, Determining grain size distribution of the material composing landslide dams in the Northern Apennines: sampling and processing methods, Eng. Geol. 69 (2003) 83–97. http://dx.doi.org/10.1016/s0013-7952(02)00249-1.

[39] C. Kang, D. Chan, Numerical simulation of 2D granular flow entrainment using DEM, Granul. Matter 20 (2018), 13. https://doi.org/10.1007/s10035-017-0782-x

[40] Abadie, S., Harris, J.C., Grilli, S.T., Fabre, R., 2012 Numerical modeling of tsunami waves generated by the flank collapse of the Cumbre Vieja Volcano (La Palma, Canary Islands): Tsunami source and near field effects. J. Geophys. Res.-Oceans 117, C05030. http://dx.doi.org/10.1029/2011JC007646.

[41] Skvortsov, A., Bornhold, B., 2007. Numerical simulation of the landslide generated tsunami in Kitimat Arm, British Columbia, Canada, 27 April 1975. J. Geophys. Res.-Earth Surf. 112, F02028. https://doi.org/10.1029/2006JF000499.

[42] W. Liu, S. He, A two-layer model for simulating landslide dam over mobile river beds, Landslides 13 (2016) 565-576. https://doi.org/10.1007/s10346-015-0585-2.

[43] P. Si, J. Aaron, S. McDougall, S., Lu, J., Yu, X., Roberts, N.J., Clague, J.J., 2018. A non-hydrostatic model for the numerical study of landslide-generated waves, Landslides 15(4), 711-726. https://doi.org/10.1007/s10346-017-0891-y.

[44] A. Armanini, Granular flows driven by gravity, J. Hydraul. Res. 51 (2013) 111-120. https://doi.org/10.1080/00221686.2013.788080.

[45] J. Li, Z. Cao, G. Pender, Q. Liu, A double layer-averaged model for dam-break flows over mobile bed, J. Hydraul. Res. 51 (2013) 518-534. https://doi.org/10.1080/00221686.2013.812047.

[46] C. Juez, J. Murillo, P. García-Navarro, 2D simulation of granular flow over irregular steep slopes using global and local coordinates, J. Comput. Phys. 255 (2013) 166-204. https://doi.org/10.1016/j.jcp.2013.08.002.

[47] G.W. Zhao, Y.J. Jiang, J.P. Qiao, Z.J. Yang, P.P. Ding, Numerical and experimental study on the formation mode of a landslide dam and its influence on dam breaching, Bull. Eng. Geol. Environ. 78 (2019) 2519-2533. https://doi.org/10.1007/s10064-018-1255-0.

[48] J. Li, Z. Cao, K. Hu, G. Pender, Q. Liu, A depth-averaged two-phase model for debris flows over erodible beds, Earth Surf. Process Landf. 43 (2018) 817-839. https://doi.org/10.1002/esp.4283.

[49] J. Li, Z. Cao, K. Hu, G. Pender, Q. Liu, A depth-averaged two-phase model for debris flows over fixed beds, Int. J. Sediment Res. 33 (2018) 462-477. https://doi.org/10.1016/j.ijsrc.2017.06.003.

[50] J. Li, Z. Cao, H. Qian, Q. Liu, G. Pender, A depth-averaged two-phase model for fluvial sediment-laden flows over erodible beds, Adv. Water Resour. 129 (2019) 338-353. https://doi.org/10.1016/j.advwatres.2017.08.014.

[51] Z. Cao, G. Pender, S. Wallis, P. Carling, Computational dam-break hydraulics over erodible sediment bed, J. Hydraul. Eng. 130 (2004) 689-703. http://dx.doi.org/10.1061/(ASCE)0733-9429(2004)130:7(689).

[52] M. Hirano, River bed degradation with armouring, T. Jpn. Soc. Civ. Eng. 195 (1971) 55-65 (in Japanese).

[53] W. Wu, Computational river dynamics, Taylor and Francis, London, UK, 2007.

[54] G. Parker, Selective Sorting and Abrasion of River Gravel. I: Theory, J. Hydraul. Eng. 117 (1991) 131-147. https://doi.org/10.1061/(ASCE)0733-9429(1991)117:2(131).

[55] G. Parker, Selective Sorting and Abrasion of River Gravel. II: Applications. J. Hydraul. Eng, 117 (1991) 150-171. https://doi.org/10.1061/(ASCE)0733-9429(1991)117:2(150).

[56] T.B. Hoey, R. Ferguson, Numerical simulation of downstream fining by selective transport in gravel bed rivers: Model development and illustration, Water Resour. Res. 30 (1994) 2251-2260. http://doi.org/10.1029/94WR00556.

[57] O. Hungr, S.G. Evans, Entrainment of debris in rock avalanches: an analysis of a long run-out mechanism, Geol. Soc. Am. Bull. 116 (2004) 1240-1252. https://doi.org/10.1130/B25362.1.

[58] Iverson, R.M., 2012. Elementary theory of bed-sediment entrainment by debris flows and avalanches. J. Geophys. Res.- Earth Surf. 117, F03006. http://doi.org/10.1029/2011JF002189.

[59] J. Richardson, W. Zaki, Sedimentation and fluidisation: Part 1, T. Inst. Chem. Eng. 32 (1954) 35-53.

[60] R.J. Zhang, J.H. Xie, Sedimentation research in China-systematic selections, China Water and Power Press, Beijing, P. R. China, 1993.

[61] R.M. Iverson, The physics of debris flows. Rev. Geophys. 35 (1997) 245-296. http://doi.org/10.1029/97RG00426.

[62] Pudasaini, S.P., 2012. A general two-phase debris flow model. J. Geophys. Res.- Earth Surf. 117(F3). https://doi.org/0.1029/2011JF002186.

[63] D. Berzi, E. Larcan, Flow resistance of inertial debris flows, J. Hydraul. Eng. 139 (2013) 187-194. https://doi.org/10.1061/(ASCE)HY.1943-7900.0000664.

[64] S.B. Savage, K. Hutter, The motion of a finite mass of granular material down a rough incline, J. Fluid Mech. 199 (1989) 177-215. http://dx.doi.org/10.1017/S0022112089000340.

[65] G. Parker, Y. Fukushima, H.M. Pantin, Self-accelerating turbidity currents. J. Fluid Mech. 171 (1986) 145-181. https://doi.org/10.1017/S0022112086001404.

[66] D. Gidaspow, Multiphase Flow and Fluidization: Continuum and Kinetic Theory Descriptions, Academic Press, San Diego, 1994.

[67] J.M.N.T. Gray, V.A. Chugunov, Particle-size segregation and diffusive remixing in shallow granular avalanches, J. Fluid Mech. 569 (2006) 365-398. http://doi.org/10.1017/S0022112006002977.

[68] K.M. Hill, D.S. Tan, Segregation in dense sheared flows: gravity, temperature gradients, and stress partitioning, J. Fluid Mech. 756 (2014) 54-88. http://doi.org/10.1017/jfm.2014.271.

[69] Cao, Z., Li, J., Pender, G., Liu, Q., 2015. Whole-process modelling of reservoir turbidity currents by a double layer-averaged model. J. Hydraul. Eng. 141(2), 04014069. http://dx.doi.org/ 10.1061/(ASCE)HY.1943-7900.0000951, 04014069.

[70] E.F. Toro, Shock-capturing methods for free-surface shallow flows, John Wiley and Sons, Chichester, UK, 2001.

[71] Z. Cao, P. Hu, K. Hu, G. Pender, Q. Liu, Modeling roll waves with shallow water equations and turbulent closure. J. Hydraul. Res. 53 (2015) 161-177. http://dx.doi.org/10.1080/00221686.2014.950350.

[72] Q.H. Liang, A.G.L. Borthwick, Adaptive quadtree simulation of shallow flows with

wet-dry fronts over complex topography. Comp. Fluids 38 (2009) 221–234. http://dx.doi.org/10.1016/j.compfluid.2008. 02.008

[73] M.W. Reeks, D. Hall, Kinetic models for particle resuspension in turbulent flows: theory and measurement. J. Aerosol Sci. 32 (2001) 1-31. https://doi.org/10.1016/S0021-8502(00)00063-X

[74] J.F. Morris, A review of microstructure in concentrated suspensions and its implications for rheology and bulk flow. Rheol. Acta 48 (2009) 909-923.

[75] C.M. Toro-Escobar, C. Paola, G. Parker, Transfer function for the deposition of poorly sorted gravel in response to streambed aggradation, J. Hydraul. Res. 34 (1996) 35-53. https://doi.org/10.1080/00221689609498763.

[76] T. Shan, J.D. Zhao, A coupled CFD-DEM analysis of granular flow impacting on a water reservoir, Ac. Mec. 225 (2014) 2449–2470. doi:10.1007/s00707-014-1119-z.

[77] G. Zitti, C. Ancey, M. Postacchini, M. Brocchini, Impulse waves generated by snow avalanches: Momentum and energy transfer to a water body, J. Geophys. Res.- Earth Surf. 121 (2016) 2399- 2423. https://doi.org/10.1002/2016JF003891.

[78] G.S. Miller, W. Andy Take, R.P. Mulligan, S. McDougall, Tsunamis generated by long and thin granular landslides in a large flume. J. Geophys. Res.- Oceans 122 (2017), 653-668. http://dx.doi.org/10.1002/2016JC012177.

[79] F. Legros, The mobility of long-runout landslides. Eng. Geol. 63 (2002) 303-331.

[80] S.F. Dal Sasso, A. Sole, S. Pascale, F. Sdao, A. Bateman Pinzón, V. Medina, Assessment methodology for the prediction of landslide dam hazard, Nat. Hazards Earth Syst. Sci. 14 (2014) 557-567. https://doi.org/10.5194/nhess-14-557-2014.

[81] F.J. Swanson, N. Oyagi, M. Tominaga, Landslide dams in Japan, in: R.L. Schuster (Eds), Landslide dams: Processes risk and mitigation, American Society of Civil Engineers, 1986, pp. 131–145.

[82] C.T. Stefanelli, S. Segoni, N. Casagli, F. Catani, Geomorphic indexing of landslide dams evolution, Eng. Geol. 208 (2016) 1-10. https://doi.org/10.1016/j.enggeo.2016.04.024

List of figure captions

Fig. 1. Experimental setup for Series 1 (adapted from Bregoli et al. [21])

Fig. 2. Granular landslide into a reservoir: DLT and DTS predictions and Bregoli et al.'s [21] measurements of temporal variations of (a) landslide velocity and (b) landslide thickness at impact with water in a basin.

Fig. 3. Granular landslide into a reservoir: DLT and DTS model predictions and Bregoli et al.'s [21] measurements of non-dimensional water level displacements with non-dimensional time water in a basin.

Fig. 4. Granular landslide into a reservoir: (a1-a4) DLT and (b1-b4) DLS model predictions of sediment concentration distributions in the basin.

Fig. 5. Granular landslide into a reservoir: (a1-a4) DLT and (b1-b4) DLS model predictions of bed deformation in the basin.

Fig. 6. Experimental setup for Series 2 (adapted from Zhao et al. [47])

Fig. 7. Valley types and geometry (adapted from Zhao et al. [47]).

Fig. 8. Schematic view of the setup for Series 3 (modified from Zhao et al. [29]).

Fig. 9. Evolution of sediment deposit lengths under different initial flow velocities.

Fig. 10. Evolution of sediment deposit heights under different initial flow velocities.

Fig. 11. Barrier lake formation: (a1-a4) landslide thickness plus bed deformation (b1-b4) water thickness, in relation to Case 3-1.

1133

1134 **Fig. 12.** Numerical setup for Series 4 (modified from Zhao et al. [47]).

1135

1136 **Fig. 13.** Barrier lake formation in relation to Case 4-1: (a1-a4) landslide thickness plus bed
1137 deformation (b1-b4) water thickness.

1138

1139 **Fig. 14.** Typical instants of the barrier lake formation in relation to Case 4-1.

1140

1141 **Fig. 15.** Velocity differences between the water and sediment phases of landslide in
1142 transverse ($y-$axis) direction, in relation to Case 3-1, a1-a4 with $d=$ 150 mm, and b1-b4
1143 with $d=$ 250 mm.

1144

1145 **Fig. 16.** Velocity differences between the water and sediment phases of landslide in
1146 longitudinal ($x-$axis) direction, in relation to Case 3-1,a1-a4 with $d=$ 150 mm, b1-b4 with
1147 $d=$ 250 mm.

1148

1149 **Fig. 17.** Evolution of sediment deposit heights under different mean diameters.

1150

1151 **Fig. 18.** Evolutions of sediment deposit heights under different grain size distributions, in
1152 relation to Case 3-1.

1153

1154 **Fig. 19.** Landslide movements and waves under a broad grain size distribution, in relation to
1155 Case 3-1: (a1-a4) landslide thickness plus bed deformation (b1-b4) water thickness.

1156

1157 **Fig.20.** Threshold for barrier lake formation as presented by computed $R_V R_\rho / \theta$ against the
1158 velocity ratio R_u along with solid circle and open square symbols respectively showing
1159 barrier lake is formed and not-formed.

1160

1161

List of table captions

Table 1 Comparisons of key physics and computational efficiency of the present and previous models

Table 2 Summary of experimental landslide dam formation and results (Series 2)

Table 3 Grain size distribution